

COLD GASS, an IRAM legacy survey of molecular gas in massive galaxies – I. Relations between H₂, H I, stellar content and structural properties

Amélie Saintonge,^{1,2*} Guinevere Kauffmann,¹ Carsten Kramer,³ Linda J. Tacconi,² Christof Buchbender,³ Barbara Catinella,¹ Silvia Fabello,¹ Javier Graciá-Carpio,² Jing Wang,^{1,4} Luca Cortese,⁵ Jian Fu,^{1,6} Reinhard Genzel,² Riccardo Giovanelli,⁷ Qi Guo,^{8,9} Martha P. Haynes,⁷ Timothy M. Heckman,¹⁰ Mark R. Krumholz,¹¹ Jenna Lemonias,¹² Cheng Li,^{6,13} Sean Moran,¹⁰ Nemesio Rodriguez-Fernandez,¹⁴ David Schiminovich,¹² Karl Schuster¹⁴ and Albrecht Sievers³

¹Max-Planck-Institut für Astrophysik, 85741 Garching, Germany

²Max-Planck-Institut für extraterrestrische Physik, 85741 Garching, Germany

³Instituto Radioastronomía Milimétrica, Av. Divina Pastora 7, Nucleo Central, 18012 Granada, Spain

⁴Center for Astrophysics, University of Science and Technology of China, 230026 Hefei, China

⁵European Southern Observatory, Karl-Schwarzschild-Str. 2, 85748 Garching, Germany

⁶Key Laboratory for Research in Galaxies and Cosmology, Shanghai Astronomical Observatory, Chinese Academy of Sciences, Nandan Road 80, Shanghai 200030, China

⁷Center for Radiophysics and Space Research, Cornell University, Ithaca, NY 14853, USA

⁸National Astronomical Observatories, Chinese Academy of Sciences, Beijing 100012, China

⁹Institute for Computational Cosmology, Department of Physics, Durham University, South Road, Durham DH1 3LE

¹⁰Johns Hopkins University, Baltimore, MD 21218, USA

¹¹Department of Astronomy and Astrophysics, University of California, Santa Cruz, CA 95064, USA

¹²Department of Astronomy, Columbia University, New York, NY 10027, USA

¹³Max-Planck-Institut Partner Group, Shanghai Astronomical Observatory, Shanghai, China

¹⁴Institut de Radioastronomie Millimétrique, 300 Rue de la piscine, 38406 St Martin d'Hères, France

Accepted 2011 March 8. Received 2011 March 7; in original form 2010 November 2

ABSTRACT

We are conducting COLD GASS, a legacy survey for molecular gas in nearby galaxies. Using the IRAM 30-m telescope, we measure the CO(1–0) line in a sample of ~ 350 nearby ($D_L \simeq 100\text{--}200$ Mpc), massive galaxies ($\log(M_*/M_\odot) > 10.0$). The sample is selected purely according to stellar mass, and therefore provides an unbiased view of molecular gas in these systems. By combining the IRAM data with Sloan Digital Sky Survey (SDSS) photometry and spectroscopy, GALEX imaging and high-quality Arecibo H I data, we investigate the partition of condensed baryons between stars, atomic gas and molecular gas in $0.1\text{--}10L^*$ galaxies. In this paper, we present CO luminosities and molecular hydrogen masses for the first 222 galaxies. The overall CO detection rate is 54 per cent, but our survey also uncovers the existence of sharp thresholds in galaxy structural parameters such as stellar mass surface density and concentration index, below which all galaxies have a measurable cold gas component but above which the detection rate of the CO line drops suddenly. The mean molecular gas fraction M_{H_2}/M_* of the CO detections is 0.066 ± 0.039 , and this fraction does not depend on stellar mass, but is a strong function of (NUV – r) colour. Through stacking, we set a firm upper limit of $M_{\text{H}_2}/M_* = 0.0016 \pm 0.0005$ for red galaxies with NUV – $r > 5.0$. The average molecular-to-atomic hydrogen ratio in present-day galaxies is

*E-mail: amelie@mpe.mpg.de

0.3, with significant scatter from one galaxy to the next. The existence of strong detection thresholds in both the H I and CO lines suggests that ‘quenching’ processes have occurred in these systems. Intriguingly, atomic gas strongly dominates in the minority of galaxies with significant cold gas that lie above these thresholds. This suggests that some re-accretion of gas may still be possible following the quenching event.

Key words: surveys – galaxies: evolution – galaxies: fundamental parameters – galaxies: ISM – radio lines: galaxies.

1 INTRODUCTION

Perhaps the most fascinating aspect of nearby galaxies is the intricately interwoven system of correlations between their global properties. These correlations form the basis of the so-called ‘scaling laws’, which are fundamental because they provide a quantitative means of characterizing how the physical properties of galaxies relate to each other. Galaxy scaling relations also provide the route to understanding the internal physics of galaxies, as well as their formation and evolutionary histories.

We currently enjoy a diverse array of scaling laws that describe the stellar components of galaxies, for example the Tully–Fisher relation for spiral galaxies (Tully & Fisher 1977), and the Fundamental Plane for ellipticals (Jorgensen, Franx & Kjaergaard 1996). Both relations provide important constraints on how these systems have assembled. However, a few well-established scaling laws exist describing how the cold gas is correlated with the other global physical properties of galaxies. The only well-studied relation is the Schmidt–Kennicutt star formation law (Kennicutt 1998), relating the formation rate of new stars and the surface density of cold gas in discs.

The reason why so few scaling laws involving cold gas and global galaxy properties, such as masses, sizes and bulge-to-disc ratios, exist in the literature, is the difficulty in acquiring suitable data. There are four general requirements on the data if the derived scaling laws are to be reliable: (1) homogeneous and accurate measurements of all the physical properties under consideration; (2) unbiased measurement of every property with respect to every other property; (3) sample selection that ensures large dynamic range of the various physical properties under consideration; (4) a large enough sample to define both the mean relation and the scatter about the mean. As we will describe, existing data sets do not, in general, meet all of these conditions.

Line emission from the CO molecule was first detected in the central parts and discs of nearby galaxies 35 years ago (Rickard et al. 1975; Solomon & de Zafra 1975; Combes et al. 1977). A decade later, CO measurements existed for ~ 100 galaxies (see the compilation of Verter 1985), and in the following years, several larger systematic studies of molecular gas in nearby galaxies were performed. The largest effort was the FCRAO Extragalactic CO Survey (Young et al. 1995), which measured the CO $J = 1 \rightarrow 0$ line [hereafter, CO(1–0)] in 300 nearby galaxies. Because of a strong correlation between infrared luminosity and CO luminosity (e.g. Sanders, Scoville & Soifer 1991; Sanders & Mirabel 1996), a significant part of this early work was done targeting luminous infrared galaxies (e.g. Radford, Downes & Solomon 1991; Solomon et al. 1997). Even the FCRAO Survey, still considered as the reference for CO measurements in the nearby Universe, targeted galaxies selected on infrared or B -band luminosity.

Recognizing this bias towards ‘exceptional’ galaxies (e.g. starbursts and interacting systems), Braine et al. (1993) observed the

CO $1 \rightarrow 0$ and $2 \rightarrow 1$ rotational transition lines with the IRAM 30-m telescope for a magnitude-limited sample of 81 normal spiral galaxies. Other attempts at measuring molecular gas in normal galaxies include the work of Kenney & Young (1988) for Virgo cluster spirals, of Sage (1993) for nearby non-interacting spirals and of Boselli et al. (1997) for Coma cluster spirals.

These pioneering studies constrained molecular gas properties in nearby galaxies as a function of morphology (e.g. Thronson et al. 1989; Wiklind & Henkel 1989), star formation rate or infrared luminosity (e.g. Sanders & Mirabel 1985; Gao & Solomon 2004), atomic gas contents (e.g. Young & Knezek 1989), environment (e.g. Kenney & Young 1989; Casoli et al. 1991; Boselli et al. 1997), and for resolved studies, position within galaxy discs. Highlights from these studies include the observations that molecular gas distributions decline monotonically with galaxy-centric radius unlike the atomic gas distributions, that IR-luminous galaxies are also CO-bright, with molecular gas concentrated within the inner kpc of these mostly interacting systems, and that the total gas mass fraction as well as the molecular-to-atomic ratio are functions of Hubble type.

Nevertheless, most of the samples did not meet all of the criteria listed above that would allow for accurate scaling laws to be derived; some samples were biased towards a particular galaxy type (e.g. infrared-bright objects), some of the more unbiased samples did not cover enough parameter space (e.g. targeting only spiral galaxies), some samples suffered from aperture problems, some samples were too small, and attempts to combine different samples to remedy these problems led to inhomogeneous data sets (see also Section 7).

Recently, much effort has been put into obtaining homogeneous and relatively deep high spatial resolution molecular gas maps covering the optical discs of nearby galaxies (Regan et al. 2001; Kuno et al. 2007; Leroy et al. 2009). These samples are excellent for studying star formation laws within galaxies (e.g. Bigiel et al. 2008), but the number of objects is too small to adequately define global scaling relations.

With reliable measurements of molecular gas for a large, unbiased sample of galaxies, it is possible not only to quantify scaling relations, but also to construct an accurate molecular gas mass function. Current estimates are based on inherently inhomogeneous samples (Keres, Yun & Young 2003; Obreschkow & Rawlings 2009). We can also investigate the molecular gas properties of galaxy samples for which dedicated surveys do exist, but where the number of objects studied has been very small, for example early-type galaxies (e.g. Combes, Young & Bureau 2007; Krips et al. 2010), and galaxies with active nuclei (e.g. Helfer & Blitz 1993; Sakamoto et al. 1999; Garcia-Burillo et al. 2003). A large unbiased sample of galaxies which can serve as a reference for such particular objects would also be very valuable.

In this paper, we introduce COLD GASS, a new survey for molecular gas in nearby galaxies. Upon completion, it will have measured fluxes in the CO(1–0) line for a purely mass-selected sample of at least 350 galaxies. The sample contains galaxies with a wide range

of Hubble types from star-forming spirals to ‘red and dead’ ellipticals. With its new, large-bandwidth receivers, the IRAM 30-m telescope is the instrument of choice to conduct a new large molecular gas survey, allowing the community to move from dedicated studies of particular types of galaxies, to larger systematic efforts. COLD GASS will provide a definitive, unbiased census of the partition of condensed baryons in the local Universe into stars, atomic and molecular gas in galaxies covering over 2 orders of magnitude in luminosity.

In Sections 2–4, we present an overview of the survey and of the sample selection, and describe the CO measurements and ancillary data sets. In Sections 5 and 6 we present the first COLD GASS scaling relations, correlating molecular gas masses with global galaxy parameters including stellar mass and atomic gas mass. Throughout the paper, distance-dependent quantities are calculated for a standard flat Λ CDM cosmology with $H_0 = 70 \text{ km s}^{-1} \text{ Mpc}^{-1}$, and we adopt a conversion factor from CO luminosity to H_2 mass of $\alpha_{\text{CO}} = 3.2 M_{\odot} (\text{K km s}^{-1} \text{ pc}^2)^{-1}$ (which does not account for the presence of helium), unless otherwise specified.

2 SURVEY DESCRIPTION AND SAMPLE SELECTION

The conditions listed in Section 1, which are required to obtain reliable scaling laws, are routinely met by optically selected samples of galaxies at a low redshift. The Sloan Digital Sky Survey (SDSS; Stoughton et al. 2002) with its five-band optical imaging campaign over a quarter of the sky and its follow-up spectroscopy of close to a million galaxies has facilitated the study of galaxy scaling relations studies at an unprecedented level of detail.

At radio wavelengths, a series of large blind H I surveys have become possible thanks to a number of new multifeed arrays. The most advanced of these, the Arecibo Legacy Fast ALFA Survey (ALFALFA; Giovanelli et al. 2005), will have detected upon completion $\sim 30\,000$ galaxies out to distances of $\sim 200 \text{ Mpc}$. Although ALFALFA measurements are accurate, homogeneous and unbiased, the survey is shallow, with the result that it does not probe a large dynamic range in H I -to-stellar mass ratio for all but the very nearest galaxies. For example, in the redshift range $0.025 < z < 0.05$, the median value of M_{HI}/M_* for ALFALFA detections with $M_* > 10^{10} M_{\odot}$ is ~ 25 per cent.

2.1 GASS

To overcome this issue, the *GALEX* Arecibo SDSS Survey (GASS; Catinella et al. 2010) was designed to measure the neutral hydrogen content for a large, unbiased sample of ~ 1000 massive galaxies ($M_* > 10^{10} M_{\odot}$), via longer pointed observations. GASS is a large programme currently under way at the Arecibo 305-m telescope, and is producing some of the first unbiased atomic gas scaling relations in the nearby Universe (Catinella et al. 2010; Schiminovich et al. 2010; Fabello et al. 2011).

Details of the GASS survey design, target selection and observing procedures are given in Catinella et al. (2010). In short, the galaxies observed as a part of GASS are selected at random out of a larger parent sample of galaxies that meet the following criteria.

- (i) They are located within the area of overlap of the SDSS spectroscopic survey, the ALFALFA survey and the projected footprint of the *GALEX* Medium Imaging Survey (MIS).
- (ii) They lie in the redshift range $0.025 < z < 0.05$.

- (iii) They have a stellar mass in the range $10^{10} < M_*/M_{\odot} < 10^{11.5}$.

The GASS sample was selected out of this parent sample to produce a flat $\log M_*$ distribution. No other selection criteria on colour, morphology or spectral properties for example were applied. This sample therefore provides us with a complete picture of how the cold atomic gas relates to other properties such as stellar mass, luminosity, stellar surface mass density or colour.

Catinella et al. (2010) present the first GASS data release, which includes ~ 20 per cent of the final sample. They show that there exist strong anticorrelations between the atomic gas mass fraction and stellar mass, stellar mass surface density and near-ultraviolet $-r$ (NUV $-r$) colour. GASS also aims at studying the galaxies that are transitioning between a blue, star-forming state and a red passive state (and vice versa). These are identified as outliers from the mean scaling relations. The ultimate goal is to understand the physical processes that affect the gas content of these galaxies (e.g. accretion or quenching) and in turn the star formation process.

2.2 COLD GASS

We are in the process of constructing a CO Legacy Data base for the GASS survey (COLD GASS), measuring the molecular gas content of a significant subsample of the GASS galaxies. We will then be able to quantify the link between atomic gas, molecular gas and stars in these systems.

COLD GASS is designed to meet all the requirements to produce reliable gas scaling relations:

- (i) Galaxies in our redshift range ($0.025 < z < 0.05$) have angular diameters that are small enough to enable accurate measurement of the total CO line flux with a single IRAM 30 m pointing for the majority (80 per cent) of the galaxies. For the remaining objects, we recover the total flux by adding a single offset pointing (see Section 4.4 for details).

- (ii) In the mass range we study ($10^{10} < M_*/M_{\odot} < 10^{11.5}$), the metallicity of the galaxies is around solar (Tremonti et al. 2004). The CO line flux therefore provides a reasonably accurate measurement of the total molecular gas content using a single conversion factor, α_{CO} .

- (iii) The ~ 350 targets are selected at random from the GASS survey, the sample is therefore unbiased.

- (iv) We integrate until the CO line is detected, or until we reach an upper limit in molecular gas mass to stellar mass ratio ($f_{\text{H}_2} \equiv M_{\text{H}_2}/M_*$) of ~ 1.5 per cent.

- (v) Upon completion of the survey, the sample size of at least 350 galaxies will be large enough to determine accurately a set of scaling laws involving three parameters and to measure the scatter around these relations.

Distributions of some basic parameters of the COLD GASS sample are shown in Fig. 1 and compared to a purely volume-limited subset of galaxies. The COLD GASS targets are selected randomly from the GASS survey and therefore share the flat $\log M_*$ distribution designed for that survey to ensure even sampling of the stellar mass parameter space. As seen in Fig. 1, a purely volume-limited sample is richer in low-mass galaxies, and poorer in high-mass systems. The uniform mass distribution also has the effect of flattening the colour distribution and reducing the number of galaxies with low stellar mass surface densities. We note that when deriving scaling relations and calculating sample averages, we statistically correct

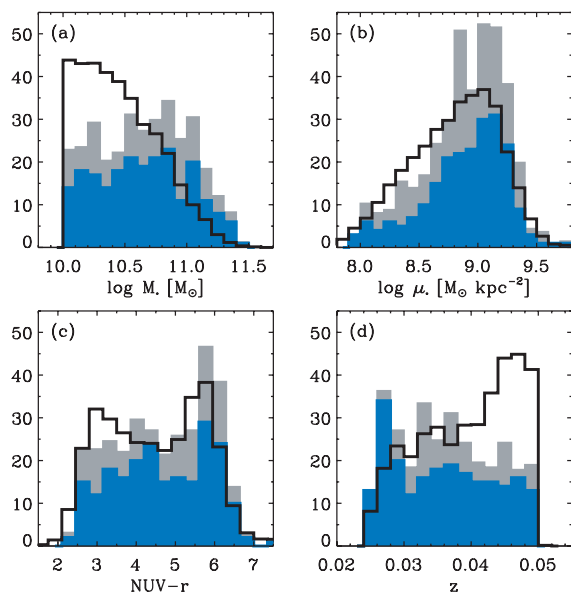


Figure 1. Distribution of sources observed as of 2010 October 25 (filled blue histograms), compared to the proposed final COLD GASS sample (filled grey histograms). The solid line in each panel shows the distribution of objects in the superset of $\sim 12\,000$ galaxies out of which the GASS sample is extracted; scaled down to the number of objects in the COLD GASS master list (350). The GASS sample is selected as to produce a flat distribution in $\log M_*$.

for this ‘mass bias’, as done by Catinella et al. (2010) for the GASS sample (see Section 5).

3 SDSS, GALEX AND Arecibo OBSERVATIONS

3.1 Optical and UV measurements

Parameters such as redshifts, sizes, magnitudes and Galactic extinction factors are retrieved from the data base of SDSS DR7 (Abazajian et al. 2009). The UV data are taken from the GALEX All-sky and Medium Imaging surveys (AIS and MIS, respectively; see Martin et al. 2005).

Table 1. Optical and UV parameters of the COLD GASS galaxies.

GASS ID	SDSS ID	z_{SDSS}	M_* ($\log M_\odot$)	μ_* ($\log M_\odot \text{ kpc}^{-2}$)	D_{25} (arcsec)	R_{90}/R_{50}	NUV $- r$ (mag)	r (mag)
11956	J000820.76+150921.6	0.0395	10.09	8.48	22.5	2.15	3.04	16.28
12025	J001934.54+161215.0	0.0366	10.84	9.13	34.3	3.03	5.93	14.73
12002	J002504.00+145815.2	0.0367	10.48	9.41	24.2	3.17	6.25	15.46
11989	J002558.89+135545.8	0.0419	10.69	9.18	23.7	3.02	5.79	15.13
27167	J003921.66+142811.5	0.0380	10.37	9.14	21.1	2.77	4.48	15.49
3189	J004023.48+143649.4	0.0384	10.05	7.92	37.7	1.96	2.77	15.65
3261	J005532.61+154632.9	0.0375	10.08	8.57	22.8	2.54	2.63	15.48
3318	J010238.29+151006.6	0.0397	10.53	8.98	26.4	3.05	5.73	15.21
3439	J010905.96+144520.8	0.0386	10.35	8.78	32.5	2.90	3.05	15.48
3465	J011221.82+150039.0	0.0292	10.19	8.93	28.7	2.89	3.63	15.33
3645	J011501.75+152448.6	0.0307	10.33	8.93	28.1	2.71	3.97	15.11
3509	J011711.65+132027.3	0.0484	10.81	9.18	31.1	3.11	4.14	15.27
3519	J011728.11+144215.9	0.0427	10.74	8.64	34.2	2.20	3.68	14.94
3505	J011746.76+131924.5	0.0479	10.21	8.83	17.7	3.30	4.92	16.35
3504	J011823.44+133728.4	0.0380	10.16	7.91	37.7	1.84	2.85	15.34

Note. Table 1 is published in its entirety in the electronic version of the journal (see Supporting Information). A portion is shown here as an example of its format and contents.

The SDSS and GALEX images are reprocessed following Wang et al. (2010), in order to obtain an accurate aperture photometry. The process includes registering the images and smoothing them to a common point spread function (PSF). The SDSS r -band images are convolved to the resolution of the UV imaging before SEXTRACTOR is used to calculate magnitudes in consistent apertures, therefore ensuring that measurements in different bands represent similar physical regions of the galaxies. The derived NUV $- r$ colours are corrected for Galactic extinction using the prescription of Wyder et al. (2007) (see also Catinella et al. 2010).

Stellar masses are calculated from the SDSS photometry using the SED-fitting technique of Salim et al. (2007), assuming a Chabrier initial mass function (IMF) (Chabrier 2003). A variety of model SEDs from the Bruzual & Charlot (2003) library are fitted to each galaxy, building a probability distribution for its stellar mass. The stellar mass assigned to a galaxy is then the mean of this distribution, while the measurement error is estimated from its width. The systematic uncertainty between different techniques to derive photometric stellar masses from SDSS measurements is < 0.1 dex, as estimated by Dutton et al. (2011).

The main optical- and UV-derived parameters used throughout this paper are presented in Table 1, for all galaxies within the present COLD GASS data release. Column 1 and 2 give the GASS and SDSS ID numbers, respectively, column 3 gives the optical redshift from SDSS spectroscopy, while column 4 lists the stellar mass and column 5 the stellar mass surface density, which we calculate as

$$\mu_* = \frac{M_*}{2\pi R_{50,z}^2}, \quad (1)$$

where $R_{50,z}$ is the z -band 50 per cent flux intensity petrosian radius, in kiloparsecs. In column 6, we give the g -band optical diameter (D_{25}), and in column 7 the concentration index ($C \equiv R_{90}/R_{50}$, where R_{50} and R_{90} are from r -band photometry). Finally, columns 8 and 9 present the NUV $- r$ colour and the r -band model magnitude, both corrected for Galactic extinction.

3.2 H I masses

Details of the H I observations are described in Catinella et al. (2010), so we only provide a brief overview here. The survey builds upon existing H I data bases: the Cornell digital H I archive

(Springob et al. 2005) and the ALFALFA survey (Giovanelli et al. 2005). H I data for about 20 per cent of the GASS sample (the most gas-rich objects), can be found in either of these sources. For the rest of the sample, observations are carried out at the Arecibo Observatory. Integration times are set such as to detect H I gas mass fractions ($f_{\text{H I}} = M_{\text{H I}}/M_*$) of 1.5 per cent or more. Observations are carried out using the *L*-band Wide receiver and the interim correlator, providing coverage of the full frequency interval of the GASS targets at a velocity resolution of 1.4 km s^{-1} before smoothing. Data reduction includes Hanning smoothing, bandpass subtraction, radio frequency interference (RFI) excision, flux calibration and weighted combination of individual spectra. Total H I-line fluxes, velocity widths and recessional velocities are then measured using linear fitting of the edges of the H I profiles (e.g. Springob et al. 2005; Catinella, Haynes & Giovanelli 2007).

4 IRAM OBSERVATIONS

4.1 Observing procedure

Observations are carried out at the IRAM 30-m telescope. We use the Eight Mixer Receiver (EMIR) to observe the CO(1–0) line (rest frequency, 115.271 GHz). The CO $1 \rightarrow 0$ transition traces well the entire molecular gas contents of the galaxies at $n(\text{H}_2) > 10^2 \text{ cm}^{-3}$ (see e.g. the appendix in Tacconi et al. 2008). In the 3-mm band (E090), EMIR offers two sidebands with 8 GHz instantaneous bandwidth per sideband and per polarization. With a single tuning of the receiver at a frequency of 111.4081 GHz, we are able to detect the redshifted CO(1–0) line for all the galaxies in our sample ($0.025 < z < 0.05$), within the 4-GHz bandwidth covered by the correlators. This single tuning procedure results in enormous time savings of 15 min per source, and in an improved relative calibration accuracy. Also, the frequency range covered benefits from a considerably improved atmospheric transmission as compared to the CO(1–0) rest frequency. The second band is tuned to a frequency of 222.8118 GHz (E230 band), to cover the redshifted CO(2–1) line which falls within the available 4-GHz bandwidth for about 75 per cent of our sample. We postpone the presentation and analysis of the CO(2–1) data until the survey is completed, to maximize the sample size.

The wobbler-switching mode is used for all the observations with a frequency of 1 Hz and a throw of 180 arcsec. The Wideband Line Multiple Autocorrelator (WILMA) is used as the back-end, covering 4 GHz in each linear polarization, for each band. WILMA gives a resolution of 2 MHz ($\sim 5 \text{ km s}^{-1}$ for the 3-mm band). We also simultaneously record the data with the 4-MHz Filterbank, as a backup.

Observations for this first data release were conducted between 2009 December and 2010 October. Atmospheric conditions varied greatly, with an average of 6 mm of precipitable water vapour (PWV). We also fold into this catalogue 15 galaxies observed in 2009 June, as a part of a pilot programme designed to test the feasibility of the survey. These galaxies were selected to be H I rich ($M_{\text{H I}}/M_* > 0.1$), but this selection bias does not affect the overall sample.

4.2 Observing strategy

Observations were carried out in fixed observing blocks and as poor-weather back-ups for higher-frequency programmes. We accommodate to the changing weather conditions by making ‘real time’ decisions on targets. We observe the bluer galaxies (generally CO-luminous) under poorer weather conditions. These galaxies require

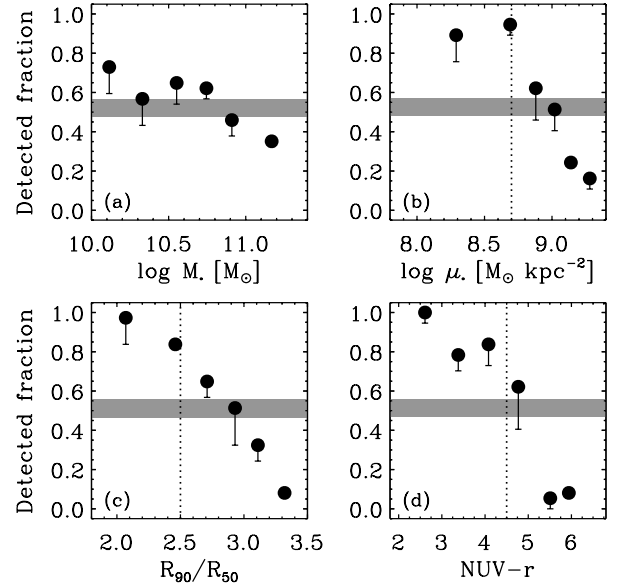


Figure 2. Fraction of galaxies with a detection in the CO(1–0) line as a function of (a) stellar mass; (b) stellar mass surface density; (c) concentration index (defined as R_{90}/R_{50} , the ratio between the *r*-band radii encompassing 90 and 50 per cent of the light); and (d) $\text{NUV} - r$ colour. The results are shown in equally populated bins, each containing 37 galaxies. The grey shaded region shows the overall detection rate of 53.6 per cent, down to 47.3 per cent if all tentative detections are excluded. The downward error bars show the effect of excluding tentative detections in each individual bin. In panels (b)–(d), the vertical dotted line indicates the critical value where the detection rate suddenly drops below ~ 80 per cent.

on average an rms sensitivity of 1.7 mK per 20 km s^{-1} -wide channel to achieve a reliable detection of the CO(1–0) line with $\text{S/N} > 5$. As seen in Fig. 2(d), galaxies with colour $\text{NUV} - r < 4.5$ have a detection rate greater than 80 per cent. When the atmospheric water vapour level is low, we preferentially observe the redder galaxies, which have a very low detection rate (Fig. 2d). In order to set firm upper limits for these galaxies, we require low noise values to reach our integration limit of $M_{\text{H}_2}/M_* = 1.5$ per cent. Under good observing conditions, sensitivity to this minimum gas fraction, or an absolute minimum rms of 1.1 mK (per 20 km s^{-1} wide channel), is reached within 1–1.5 h. This absolute minimum rms is imposed in order to keep the integration time per galaxy $< 2 \text{ h}$, and translates in a detection limit that is higher than the nominal value of 1.5 per cent for galaxies with $\log M_*/M_\odot < 10.6$.

The efficiency of the observations is also maximized by our single tuning approach (see Section 4.1), and by the fact that the galaxies are mostly concentrated in a declination strip with $0^\circ < \delta < +15^\circ$, as shown in Fig. 3. Not only does this allow us to move quickly from one source to the next without repeating pointing correction measurements, it makes it possible to almost always observe at elevations larger than 45° , minimizing atmospheric opacity.

4.3 Data reduction

The data are reduced with the CLASS software. All scans are visually examined, and those with distorted baselines, increased noise due to poor atmospheric conditions, or anomalous features are discarded. The individual scans for a single galaxy are baseline-subtracted (first-order fit) and then combined. This averaged spectrum is finally binned to a resolution of $\sim 20 \text{ km s}^{-1}$, and the standard deviation of the noise per such channel is recorded (σ_{rms}).

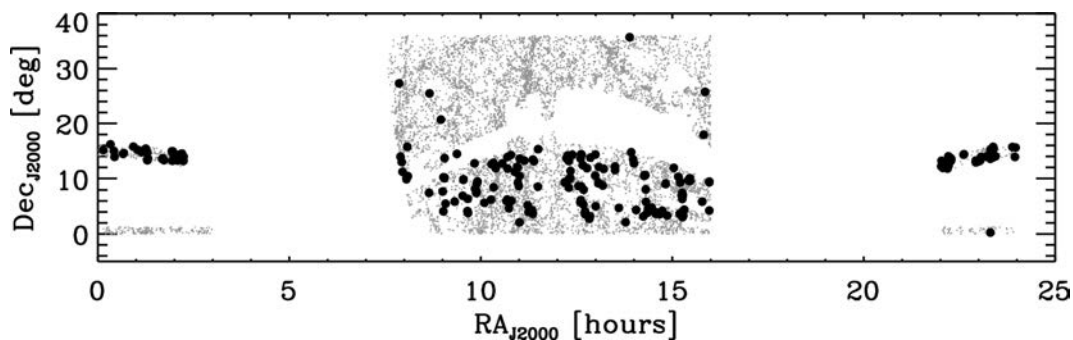


Figure 3. Sky distribution of the COLD GASS sample. Galaxies are selected in the area of intersection of the SDSS, *GALEX* MIS and ALFALFA H I surveys. Grey dots show all the 12 000 galaxies satisfying the GASS selection criteria (see Section 2.1) within the SDSS + *GALEX* footprints, and the circles represent the 222 COLD GASS galaxies that are part of this data release.

Flux in the CO(1–0) line is measured by adding the signal within an appropriately defined windowing function. If the line is detected, the window is set by hand to match the observed line profile. If the CO line is undetected or very weak, the window is set either to the full width of the H I line ($W50_{\text{H I}}$) or to a width of 300 km s^{-1} in case of an H I non-detection. For the non-detection, an upper limit for the flux of $5\epsilon_{\text{obs}}$ (see equation 5) is set.

The central velocity and total width of the detected CO lines are then measured using a custom-made IDL interactive script. The peaks of the signal are identified, and a linear fit is applied to each side of the profile between the 20 and 80 per cent peak flux level. The width of the line, $W50_{\text{CO}}$, is then measured as the distance between the points on each of the fits corresponding to 50 per cent of the peak intensity. The recession velocity is taken as the mid-point of this line. This method is described in Springob et al. (2005) and Catinella et al. (2007), and is also used to measure the H I linewidths of the GASS sample.

4.4 Aperture corrections

Because the galaxies targeted are at a distance of at least 100 Mpc ($z > 0.025$), most of them can be observed with a single pointing of the IRAM 30 m, which has a beam with an FWHM of 22 arcsec at a wavelength of 3 mm. However, some of the galaxies have optical diameters in excess of this, and an aperture correction needs to be applied.

We derive aperture corrections using a set of nearby galaxies with accurate CO maps (Kuno et al. 2007). We simulate the impact of observing galaxies with the IRAM beam by taking each of the maps, placing it at different redshifts in the range $0.025 < z < 0.05$ and computing the ratio between the flux as would be measured by a 22-arcsec Gaussian beam to the total flux in the map ($S_{\text{CO,obs}}/S_{\text{tot}}$). We find that a single central observation recovers most (>60 per cent) of the CO line flux in galaxies with $D_{25} < 40$ arcsec. Results are shown in Fig. 4(a). Based on the best fit to these data, we apply the following aperture correction:

$$S_{\text{CO,cor}} = S_{\text{CO,obs}} / (1.094 - 0.008D_{25} + 2.0 \times 10^{-5}D_{25}^2), \quad (2)$$

where $S_{\text{CO,obs}}$ is the observed flux in the central pointing and $S_{\text{CO,cor}}$ the extrapolated total flux.

For galaxies with optical diameters larger than 40 arcsec, however, there is a significant scatter in the $S_{\text{CO,obs}}/S_{\text{tot}}$ ratio, and additional information is required to recover the total CO line flux. In the right-hand panel of Fig. 4, we show that with a single offset pointing at the three-quarter beam from the central position ($0.75 \times$

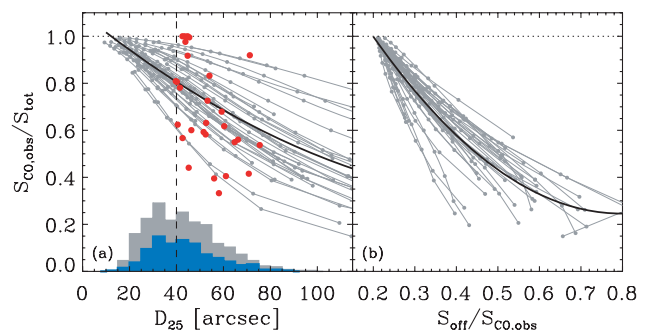


Figure 4. Aperture corrections for the IRAM 30-m observations of the COLD GASS sample. (a) Ratio between the flux recovered by a central pointing with the IRAM 22-arcsec beam to the total flux of the galaxy ($S_{\text{CO,obs}}/S_{\text{tot}}$), as a function of optical diameter (D_{25}). Small grey points indicate the results from the simulated observations of a sample of 40 nearby spiral galaxies with high-quality CO(1–0) maps (Kuno et al. 2007) when they are placed at various redshifts in the range 0.01–0.05 (each set of points connected by a broken line corresponds to one of the galaxies, placed at different redshifts). A single central pointing recovers at least 60 per cent of the flux in galaxies with $D_{25} < 40$ arcsec. The histogram indicates the size distribution of the COLD GASS sample (with the distribution of blue galaxies, $\text{NUV} - r < 4.3$, indicated in blue). (b) With an additional offset observation 0.75 beam (i.e. 16 arcsec) from the centre of the galaxy along the major axis (S_{off}), it is possible to derive the fraction of CO(1–0) line flux detected at the centre and from that estimate the total molecular gas mass in galaxies with $D_{25} > 40$ arcsec. The large red symbols in panel (a) indicate the aperture corrections estimated using this method for the 25 COLD GASS galaxies for which we performed offset pointings to date, and the dashed line is the size threshold (40 arcsec) for a galaxy to require an offset pointing.

22 arcsec^2) along the major axis, the total flux can be recovered with much better accuracy.¹ An offset pointing at a full beam also does well, but the mean ratio $S_{\text{off}}/S_{\text{CO,obs}}$ then drops from 33 to 15 per cent. We adopted the three-quarter beam offset as a compromise between the requirements for independent flux measures and a modest fraction of our total observing time going into off-centre pointings.

¹ During the pilot observations of 2009 June, we took offset pointings one full beam from the central position. These galaxies are identified clearly by asterisks in column 6 of Table 2, and aperture corrections are performed using a version of equation (3) appropriate for these larger offsets.

Our requirement to perform an offset pointing is that a galaxy has (1) a large angular size ($D_{25} > 40$ arcsec) and (2) a bright CO line in the central pointing, such that a detection in the offset pointing can be made with an hour of integration or less. For these galaxies, the flux in the central pointing is corrected based on the ratio between the flux in the offset pointing to that in the centre ($f_{\text{off}} \equiv S_{\text{off}}/S_{\text{CO,obs}}$), based on the best fit to data in Fig. 4(b):

$$S_{\text{CO,cor}} = S_{\text{CO,obs}} / (1.587 - 3.361 f_{\text{off}} + 2.107 f_{\text{off}}^2). \quad (3)$$

If a galaxy is larger than 40 arcsec but the CO line in the central pointing is weak or undetected, then the measured central flux is corrected according to equation (2).

So far, we have performed offset pointings for 25 galaxies, that met the requirements listed above (see Fig. A4). We used equation (3) and Fig. 4(b) to infer the fraction of the total flux that was measured in the central pointing ($S_{\text{CO,obs}}/S_{\text{tot}}$), and we show in Fig. 4(a) how this ratio depends on D_{25} and how it compares to the range of values predicted by our simulated observations.

4.5 M_{H_2} and associated error budget

After correcting the CO(1–0) line fluxes for aperture effects using either equation (2) or equation (3), whichever case applies to each galaxy, we compute the total CO luminosities following Solomon et al. (1997):

$$L'_{\text{CO}} = 3.25 \times 10^7 S_{\text{CO,cor}} \nu_{\text{obs}}^{-2} D_L^2 (1+z)^{-3}, \quad (4)$$

where $S_{\text{CO,cor}}$ in units of Jy km s^{-1} is the integrated line flux;² ν_{obs} is the observed frequency of the CO(1–0) line in GHz; D_L is the luminosity distance in units of Mpc; and L'_{CO} is the CO luminosity in $\text{K km s}^{-1} \text{pc}^2$.

The total molecular hydrogen masses are then calculated as $M_{\text{H}_2} = L'_{\text{CO}} \alpha_{\text{CO}}$. We adopt a constant Galactic conversion factor of $\alpha_{\text{CO}} = 3.2 M_{\odot} (\text{K km s}^{-1} \text{pc}^2)^{-1}$, which does not include a correction for the presence of helium. Our choice of α_{CO} is roughly the mean of values estimated in the Milky Way and in nearby galaxies (e.g. Strong & Mattox 1996; Dame, Hartmann & Thaddeus 2001; Blitz et al. 2007; Draine et al. 2007; Heyer et al. 2009; Abdo et al. 2010). The virial method used to measure α_{CO} has been validated by other independent techniques such as γ -ray observations, and shown to also hold for the ensemble average of the virialized clouds of entire galaxies, as long as the factor $n(\text{H}_2)^{0.5}/T$ is constant throughout the galaxy and the CO line is optically thick (Dickman, Snell & Schloerb 1986; Tacconi et al. 2010).

This constant value for α_{CO} has been shown to hold for galaxies in the Local Group, when the metallicity goes from solar down to SMC values (Bolatto et al. 2008). It may be that the conversion factor is instead a function of a parameter such as gas surface density or metallicity (Tacconi et al. 2008; Obreschkow & Rawlings 2009). Based on the well-known metallicity–luminosity relation, Boselli, Lequeux & Gavazzi (2002) for example proposed a luminosity-dependent conversion factor. However, such a prescription has yet to be observationally or theoretically validated. Furthermore, it has since been shown that the mass–metallicity relation is even more fundamental (Tremonti et al. 2004). At stellar masses above $\sim 10^{10.5} M_{\odot}$, the relation flattens out, and therefore the metallicity

² Calculated from antenna temperature units using the conversion $S/T_a^* = 6.0 \text{ Jy K}^{-1}$, specific for the IRAM 30 m at our observing frequency of 111 GHz.

of our COLD GASS galaxies is expected to be \sim solar with little variations across the sample. This expectation is confirmed by our long-slit spectroscopy measurements (Moran et al. 2010; Saintonge et al. 2011). Based on this fact, adopting a constant Galactic conversion factor $\alpha_{\text{CO}} = 3.2 M_{\odot} (\text{K km s}^{-1} \text{pc}^2)^{-1}$ is the simplest yet most justified assumption we can make at this point. We however consider the variations in α_{CO} by a factor of ~ 2 at fixed metallicity (Bolatto et al. 2008) as the systematic uncertainty on our values of M_{H_2} .

We calculate the formal measurement error on the observed line flux, $S_{\text{CO,obs}}$, as

$$\epsilon_{\text{obs}} = \frac{\sigma_{\text{rms}} W50_{\text{CO}}}{\sqrt{W50_{\text{CO}} \Delta w_{\text{ch}}^{-1}}}, \quad (5)$$

where σ_{rms} is the rms noise per spectral channel of width $\Delta w_{\text{ch}} = 21.57 \text{ km s}^{-1}$ and $W50_{\text{CO}}$ is the FWHM of the CO(1–0) line. This definition takes into account that for a given total flux, the S/N per channel is largest when the emission line is narrower. Considering all detections, the mean fractional error ($\epsilon_{\text{obs}}/S_{\text{CO,obs}}$) is 11 per cent.

Other contributions to the error budget on M_{H_2} include a flux calibration error (10 per cent at a wavelength of 3 mm, under average atmospheric conditions) and the uncertainty on the aperture correction (which we estimate to be 15 per cent based on Fig. 4 for the median galaxy in our survey). The average pointing rms error is $\Delta_{\text{point}} = 2$ arcsec, and also contributes to the uncertainty on the measured flux. Using the resolved CO(1–0) maps of Kuno et al. (2007), we simulate the observation of COLD GASS galaxies both with a beam perfectly centred on the object, and with a beam offset by Δ_{point} from the centre. We find that a 2-arcsec positional error generates a 2.1 per cent uncertainty on the measured line flux. Given that the redshift error is negligible compared to these other contributions, the fractional error on L'_{CO} is obtained by adding in quadrature all error contributions to $S_{\text{CO,cor}}$. We therefore find a mean error of $\langle \epsilon_{L_{\text{CO}}} \rangle \simeq 20$ per cent. The random measurement error on our quoted values of M_{H_2} is then ~ 20 per cent, to which we add the systematic error coming from the uncertainty in the value of α_{CO} bringing the total error on $\log M_{\text{H}_2}$ to 0.3 dex.

4.6 Stacking

To extract information from the CO non-detections, we also perform a stacking analysis. We stack the spectra after converting them in ‘gas fraction’ units following Fabello et al. (2011), who provide an extensive discussion of the merits of this technique. We convert each spectrum S into a scaled spectrum S_{gf} :

$$S_{\text{gf}} = \frac{S D_L^2}{M_* (1+z)^3}, \quad (6)$$

where the factor $D_L^2 (1+z)^{-3}$ is a consequence of equation (4). This gives us scaled spectra in units of $\text{mJy Mpc}^2 M_{\odot}^{-1}$.

For any subsample of N galaxies with CO non-detection, we calculate a mean stacked spectrum:

$$S_{\text{stack}} = \frac{\sum_{i=1}^N w_i S_{\text{gf},i}}{\sum_{i=1}^N w_i}, \quad (7)$$

where w is the weight given to each galaxy in the stack, based on its stellar mass, in order to compensate for the fact that the $\log M_*$ distribution of the COLD GASS sample is by design flatter than in a complete volume-limited sample (Fig. 1a).

Table 2. Molecular gas masses and CO(1–0) parameters for the COLD GASS galaxies.

GASS ID	σ (mK)	S/N	$S_{\text{CO,obs}}$ (Jy km s ⁻¹)	$S_{\text{CO,cor}}$ (Jy km s ⁻¹)	f_{off}	M_{H_2} (log M _⊙)	M_{H_2}/M_*	Flag
11956	1.07	2.35	1.16	1.25	...	8.46	0.024	1
12025	1.06	8.78	0.009	2
12002	1.18	8.79	0.021	2
11989	1.07	8.79	0.013	2
27167	1.17	8.74	0.023	2
3189	1.24	6.69	3.19	3.88	...	8.93	0.076	1
3261	1.96	8.57	4.27	4.62	...	8.98	0.080	1
3318	1.03	8.81	0.019	2
3439	1.03	8.79	0.028	2
3465	1.17	4.28	2.89	3.28	...	8.62	0.027	1
3645	1.08	8.62	0.020	2
3509	1.15	7.24	5.02	5.80	...	9.30	0.031	1
3519	1.53	7.72	5.51	6.52	...	9.24	0.032	1
3505	1.30	8.93	0.052	2
3504	1.53	9.19	2.83	3.44	...	8.87	0.051	1

Note. Table 2 is published in its entirety in the electronic version of the journal (see Supporting Information). A portion is shown here as an example of its format and contents.

To obtain $\langle M_{\text{H}_2}/M_* \rangle$, the mean molecular gas mass fraction for the family of N galaxies stacked, we measure a line flux or set an upper limit as described in Section 4.3, and multiply by the constant factors $3.25 \times 10^7 v_{\text{obs}}^{-2} \alpha_{\text{CO}}$ to obtain the dimensionless mass fraction.

4.7 Catalogue presentation

In Table 2, we summarize the results of the IRAM observations of the first 222 COLD GASS galaxies (119 CO detections and 103 non-detections). The contents of the catalogue are as follows.

Column (1): GASS ID. Galaxies are in the same order as in Table 1 to ease cross-referencing.

Column (2): rms noise per channel in mK, after binning the spectra to a resolution of $\Delta v_{\text{ch}} = 21 \text{ km s}^{-1}$.

Column (3): signal-to-noise ratio of the detected CO line, calculated as $S_{\text{CO,obs}}/\epsilon_{\text{obs}}$, where ϵ_{obs} is calculated according to equation (5). In our analysis, we consider sources with $S/N > 5$ as secure, and the detections with $S/N < 5$ as tentative.

Column (4): integrated CO line flux in Jy km s⁻¹. The measured flux in antenna temperature units is converted to these units using the ratio $S/T_a^* = 6.0 \text{ Jy K}^{-1}$ for the IRAM 30-m telescope at our observing frequency of 111 GHz.

Column (5): corrected total line flux in Jy km s⁻¹, computed following equations (2) and (3).

Column (6): when available, the measured ratio between the flux in the offset pointing to that in the central pointing, as described in Section 4.4.

Column (7): total molecular hydrogen gas mass. We adopt a constant Galactic conversion factor of $\alpha_{\text{CO}} = 3.2 \text{ M}_{\odot} (\text{K km s}^{-1} \text{ pc}^2)^{-1}$, which does not include a correction for the presence of helium. The numbers quoted are either measured masses in the case of detections, or 5σ upper limits for the non-detections (see column 9).

Column (8): molecular gas mass fraction, $f_{\text{H}_2} \equiv M_{\text{H}_2}/M_*$, and upper limits for non-detections.

Column (9): CO emission line flag, set to 1 for detections and 2 for non-detections.

5 MOLECULAR GAS FRACTION SCALING RELATIONS

5.1 Molecular gas fraction and global galaxy parameters

We first investigate how the molecular gas mass fraction³ ($f_{\text{H}_2} \equiv M_{\text{H}_2}/M_*$) varies across the COLD GASS sample. The values of f_{H_2} range from 0.009 (G7286), at the very edge of the survey's detection limit, up to 0.20 for the most H_2 -rich galaxy in the sample observed so far (G41969). Overall, the molecular gas contents are more modest, averaging at $\langle f_{\text{H}_2} \rangle = 0.066 \pm 0.039$ for the CO detections, and at 0.043 ± 0.022 when non-detections are included in the mean at the value of their upper limits. These sample averages are measured by weighting each galaxy differently according to its stellar mass, in order to compensate for the flat $\log M_*$ distribution (see Section 5.2 for more details).

In Fig. 5, we investigate how the molecular gas mass fraction depends on stellar mass, stellar mass surface density, concentration index and NUV – r colour. For all four relations, we quantify the strength of the dependence of f_{H_2} on the x -axis parameter in two ways. First, we compute for all secure detections the Pearson correlation coefficient of the relation, r . Secondly we perform an ordinary least-squares linear regression of f_{H_2} on the x -axis parameter for the secure detections, and report the standard deviation of the residuals about this best-fitting relation, σ , in $\log M_{\text{H}_2}/M_*$ units.

There is a weak dependency of f_{H_2} on stellar mass, M_* , as seen in Fig. 5(a), with a correlation coefficient $r = -0.40$, and a scatter of $\sigma = 0.292$ dex, but some of this correlation is caused by the detection limit. The strength of the correlation of f_{H_2} on stellar mass surface density, μ_* , is similar with $r = -0.33$ and $\sigma = 0.301$ dex (Fig. 5b). There is however a striking difference in the behaviour of the non-detections; while the detection rate is roughly constant as a function of M_* (~ 50 per cent; see Fig. 2a), it is a strong function of μ_* . There is a surface density threshold of $\mu_* \simeq 10^{8.7} \text{ M}_{\odot} \text{ kpc}^{-2}$, below which the detection rate is almost 100 per cent and above which it quickly drops. A similar threshold is observed by Catinella et al. (2010) in

³ We warn the reader that our definition of f_{H_2} differs from some previous studies, where f_{H_2} is also defined as $M_{\text{H}_2}/M_{\text{dyn}}$ or $M_{\text{H}_2}/(M_* + M_{\text{H}_1} + M_{\text{H}_2})$.

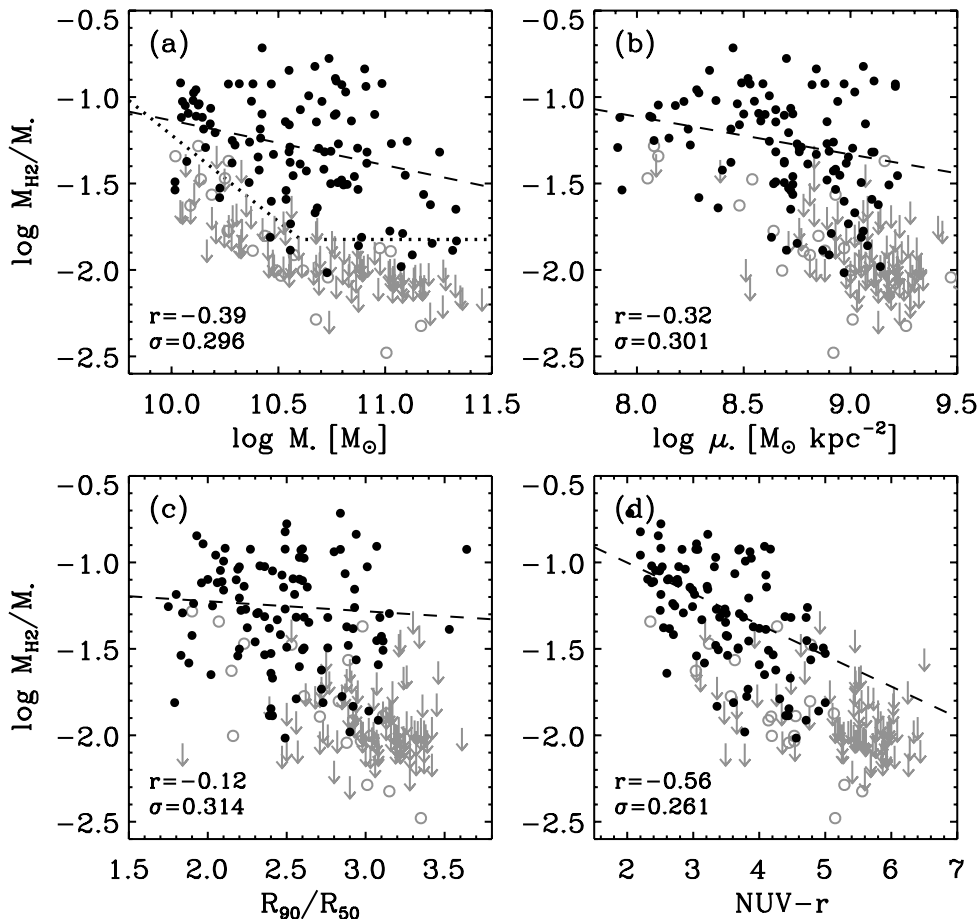


Figure 5. Molecular gas mass fraction ($f_{\text{H}_2} \equiv M_{\text{H}_2}/M_*$) as a function of (a) stellar mass, (b) stellar mass surface density, (c) concentration index R_{90}/R_{50} and (d) $\text{NUV} - r$ colour. Detections in CO are shown as circles (filled: $S/N > 5$, open: $S/N < 5$), and upper limits obtained for non-detections as arrows. In panel (a), the dotted line represents the detection limit of the survey, which is a function of M_* at the low-mass end due to the hard limit of 1.1 mK for the observed rms (see Section 4.2 for details). In each panel, we give the value of the Pearson correlation coefficient of the relation (r), and the standard deviation σ about the best-fitting linear relation to all CO detections (dashed line).

the relation between the atomic gas mass fraction ($f_{\text{H}_1} \equiv M_{\text{H}_1}/M_*$) and μ_* (see Section 6 for more details).

To test the impact of galaxy morphology on the molecular mass fraction, we plot in Fig. 5(c) f_{H_2} as a function of the concentration index, defined as $C \equiv R_{90}/R_{50}$ where R_{90} and R_{50} are the radii enclosing 90 and 50 per cent of the r -band flux, respectively. The concentration index is a good proxy for the bulge-to-total ratio, as would be recovered by full two-dimensional bulge/disc decompositions (Weinmann et al. 2009). The galaxies with a CO line detection show no correlation, with a correlation coefficient of -0.14 , and a scatter about the best-fitting relation (0.317 dex) as large as the scatter in f_{H_2} itself (also 0.317 dex), suggesting that the presence of a bulge does not affect strongly how much of the mass in these galaxies is in the form of molecular gas. A similar result was found by Catinella et al. (2010) and Fabello et al. (2011) for the H I contents of similar galaxies. The only effect seen is again in the detection fraction, with the success rate of measuring the CO line dropping sharply from 100 per cent for the most disc-dominated systems, to 0 per cent for the most bulge-dominated ones.

The only parameter upon which the measured molecular mass fractions does depend significantly is colour ($r = -0.57$, $\sigma = 0.260$ dex; see Fig. 5d). Since $\text{NUV} - r$ colour is a proxy for specific star formation rate, this dependency of f_{H_2} is expected, because star formation and molecular gas are known to be strongly correlated. It

is interesting to note that not a single red sequence galaxy ($\text{NUV} - r > 5.0$) has a measurable molecular gas component ($f_{\text{H}_2} < 0.015$ in all cases). To test this further, we stack all non-detections with $\text{NUV} - r > 5$ using the technique described in Section 4.6. The result is shown in Fig. 6. Even in the stack, the red galaxies lead to a non-detection of the CO line, thus setting an even more restrictive upper limit on the molecular gas mass fraction of 0.0016 ± 0.0005 , which at their median stellar mass corresponds to an upper limit on the molecular gas mass of $\sim 1.1 \times 10^8 M_{\odot}$. Molecular gas has been detected in early-type galaxies (e.g. in the SAURON sample, Combes et al. 2007), but at levels even below this limit. Our results are therefore not in contradiction with these studies.

5.2 Mean scaling relations

After having looked separately at the properties of CO detections and non-detections as a function of several global galaxy parameters (Fig. 5), we combine all measurements into mean molecular gas mass fraction scaling relations.

As described in Section 2.2, the COLD GASS sample has been generated to have a stellar mass distribution that is flatter than it is in a purely volume-limited sample (see Fig. 1). When building the scaling relations, we correct for this by weighing each point according to its stellar mass. Following Catinella et al. (2010),

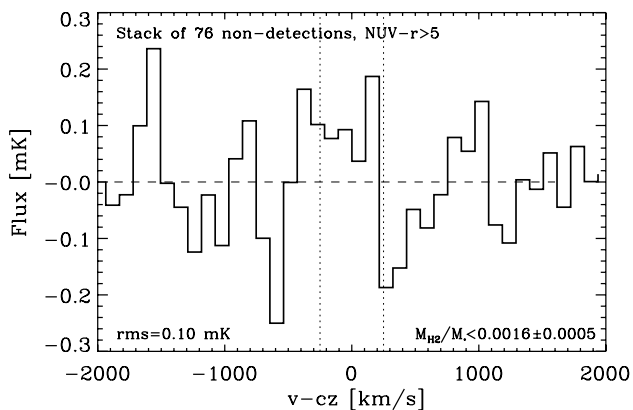


Figure 6. Stacked spectrum of all galaxies with $\text{NUV} - r > 5.0$. Individually, the galaxies included are all non-detections in CO, and even their stacked average does not yield a detection, setting instead a stringent upper limit of $\langle M_{\text{H}_2}/M_* \rangle = 0.0016 \pm 0.0005$. The vertical dotted line shows an expected linewidth of $\sim 500 \text{ km s}^{-1}$ for such a stacked signal.

the galaxies are placed in bins of stellar mass of width 0.2 dex and assigned as a weight the ratio between the total number of galaxies in the unbiased volume-limited parent sample and the total number of COLD GASS galaxies within that same mass bin. In other words, low-mass galaxies are given a higher weight in the computation of the mean scaling relations, because these galaxies are under-represented in the COLD GASS sample compared to a volume-limited sample.

Each scaling relation is computed and plotted using three different subsamples: (1) only the galaxies with CO detections are considered; (2) both the detections and non-detections are used, and the upper limit on f_{H_2} is used for the non-detections; and (3) both the detections and non-detections are used, but this time a value of $f_{\text{H}_2} = 0.0$ is assigned to the non-detections. In all cases, the weighted mean of $\log f_{\text{H}_2}$ is then calculated in equally populated bins of either M_* , μ_* , concentration index or $\text{NUV} - r$ colour, and the relations are fitted, weighting galaxies according to their stellar mass. The resulting mean relations are plotted in Fig. 7, with the error bars representing the uncertainty on the position of $\langle \log f_{\text{H}_2} \rangle$ in equally populated bins, as determined by bootstrapping: the error is the standard deviation in the value of $\langle \log f_{\text{H}_2} \rangle$ for 1000 resamples of the original data in each bin, with repetitions. The best-fitting

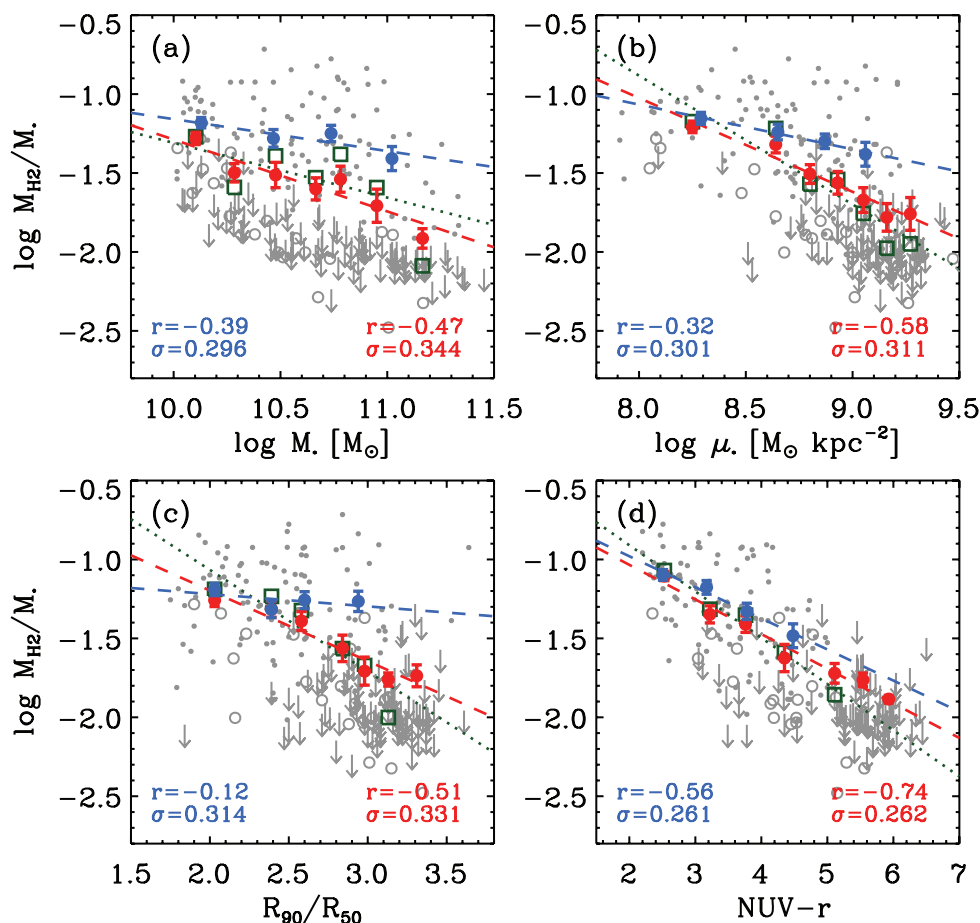


Figure 7. Molecular gas mass fraction scaling relations. The weighted mean values of $\log f_{\text{H}_2}$ in equally populated bins are plotted as a function of (a) stellar mass, (b) stellar mass surface density, (c) concentration index R_{90}/R_{50} and (d) $\text{NUV} - r$ colour. The blue circles include only CO detections. The red circles and green squares include both detections and non-detections, but differ in the way the latter are treated. We assign to the non-detections either the value set by the upper limit (red circles), or simply set them to zero (green squares). The correlation coefficients (r) and scatter around the best-fitting relation are given for detections only (lower-left corners) and for the ‘non-detections as upper limits’ case (lower-right corners). The grey symbols show the data for all COLD GASS galaxies within this data release (as presented in Fig. 5).

Table 3. Mean molecular gas fraction scaling relations.

x	x_0	(1) Detections only		(2) All, non-detections = limit		(3) All, non-detections = 0	
		m	b	m	b	m	b
$\log M_*$	10.70	-0.202 ± 0.040	-1.300 ± 0.592	-0.455 ± 0.069	-1.607 ± 1.034	-0.346 ± 0.203	-1.552 ± 3.038
$\log \mu_*$	8.70	-0.283 ± 0.019	-1.265 ± 0.237	-0.595 ± 0.055	-1.441 ± 0.682	-0.816 ± 0.127	-1.454 ± 1.587
R_{90}/R_{50}	2.50	-0.078 ± 0.048	-1.258 ± 0.176	-0.447 ± 0.049	-1.420 ± 0.185	-0.644 ± 0.145	-1.388 ± 0.529
$\text{NUV} - r$	3.50	-0.197 ± 0.012	-1.275 ± 0.066	-0.219 ± 0.013	-1.363 ± 0.077	-0.293 ± 0.013	-1.349 ± 0.069

Note. The relations are parametrized as $\log M_{\text{H}_2}/M_* = m(x - x_0) + b$.

linear relations are also plotted and summarized in Table 3. Note that in case (3), because of the null values of f_{H_2} for the non-detections, we cannot directly average and fit the values of $\log f_{\text{H}_2}$ as we do for cases (1) and (2). Instead, we measure the logarithm of the mean value of f_{H_2} in each bin, and fit these average values. This is the relation plotted in Fig. 7 and given in Table 3 for case (3).

The choice between setting the non-detections to their upper limits or to a constant value of zero only significantly affects the scaling relations at large values of μ_* , C and $\text{NUV} - r$ where few galaxies have a detected CO line. Both sets of scaling relations are included in Table 3, labelled as $\langle \log M_{\text{H}_2}/M_{\odot} \rangle_{\text{lim}}$ and $\langle \log M_{\text{H}_2}/M_{\odot} \rangle_0$ for the upper limit and zero value cases, respectively.

The mean molecular gas mass fraction is a roughly constant function of stellar mass, both for detections alone and when including non-detections, as shown in Fig. 7(a). This is a consequence of the flat detection rate of the CO line as a function of M_* . Adding non-detections turns the mostly flat relations between f_{H_2} and both μ_* and C into monotonically decreasing functions. The strongest correlation is still with $\text{NUV} - r$ colour, both before and after including non-detections. Because $\text{NUV} - r$ colour is a proxy for specific star formation rate, its correlation with f_{H_2} is not surprising, given e.g. the Kennicutt–Schmidt relation. The correlation of f_{H_2} with $\text{NUV} - r$ could therefore be seen as a consequence rather than a cause.

For the other parameters describing the underlying properties of the galaxies, independently of the current star formation rate (M_* , μ_* , concentration index), there is very little dependence of the measured values of f_{H_2} . In Section 5.1, we showed that no matter their stellar mass, about half of our sample has detectable CO line emission, which converts into a molecular mass fraction of ~ 6 per cent across the stellar mass interval sampled. On the other hand, while the molecular mass fraction of *detected* galaxies is mostly independent of μ_* , the detection fraction is a strong function of that quantity. These observations trace a picture where (1) the conditions required for the formation/consumption of molecular gas are a strong function of μ_* (and concentration index) but not of M_* , but (2) when these conditions are met, a roughly constant fraction of the stellar mass is found in the form of molecular gas.

6 THE RELATIONSHIP BETWEEN H I AND H₂

Under the assumption that molecular gas forms out of lower density clouds of atomic gas, one might naïvely expect a tight correlation between $M_{\text{H I}}$ and M_{H_2} . The actual situation is, however, quite different, as seen in Fig. 8. Within the subsample of galaxies detected both in H I and in CO, the fraction $M_{\text{H}_2}/M_{\text{H I}}$ varies greatly, from 0.037 (G13775) up to 4.09 (G38462). For galaxies with both CO and H I detections, the correlation coefficient between $\log M_{\text{H I}}$ and $\log M_{\text{H}_2}$ is $r = 0.37$, indicating that the two quantities are only weakly correlated. A bisector linear fit to the same subsample re-

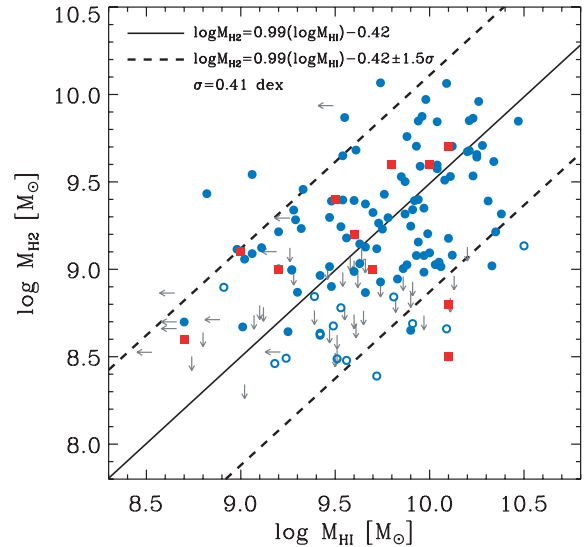


Figure 8. Comparison between atomic and molecular hydrogen gas masses. COLD GASS galaxies with detections of both the H I and CO lines are plotted as filled and open blue circles, for secure and tentative CO detections, respectively. The arrows show limits in the cases of non-detection of either the H I or the CO line. The best bisector linear fit to the detections is shown as a solid line, and the $\pm 1.5\sigma$ region around this fit is marked with dashed lines. For comparison, we overplot as filled squares the integrated measurements for the HERACLES galaxies with $M_* > 10^{10} M_{\odot}$, taken from Leroy et al. (2008).

veals that on average, M_{H_2} is 0.295 times the value of $M_{\text{H I}}$, with a large scatter of 0.41 dex in $\log(M_{\text{H}_2}/M_{\text{H I}})$ (see Fig. 8).

To further investigate the relationship between M_{H_2} and $M_{\text{H I}}$, we look into how the ratio between these two quantities varies as a function of different physical parameters. We define the molecular fraction as the ratio between the molecular hydrogen gas mass and the atomic gas mass of the system:

$$R_{\text{mol}} = \log \left(\frac{M_{\text{H}_2}}{M_{\text{H I}}} \right). \quad (8)$$

In Fig. 9, we plot R_{mol} as a function of the same four global parameters as in the previous figures. Galaxies with non-detections in both H I and H₂ are not plotted, as R_{mol} is completely unconstrained in these cases. The best-fitting linear relations, taking into account the weights correcting for the flat $\log M_*$ distribution, are measured in two ways: (1) including only the secure detections in H I and H₂ and (2) including the non-detections in either of these quantities as lower or upper limits, respectively. In Fig. 9, we also report the Pearson correlation coefficients and the scatter around these relations. The best-fitting scaling relations are given the form $R_{\text{mol}} = m(x - x_0) + b$, with the parameters presented in Table 4.

The first panel shows that R_{mol} is a very weakly increasing function of M_* ($r = 0.23$). Both with and without the non-detections

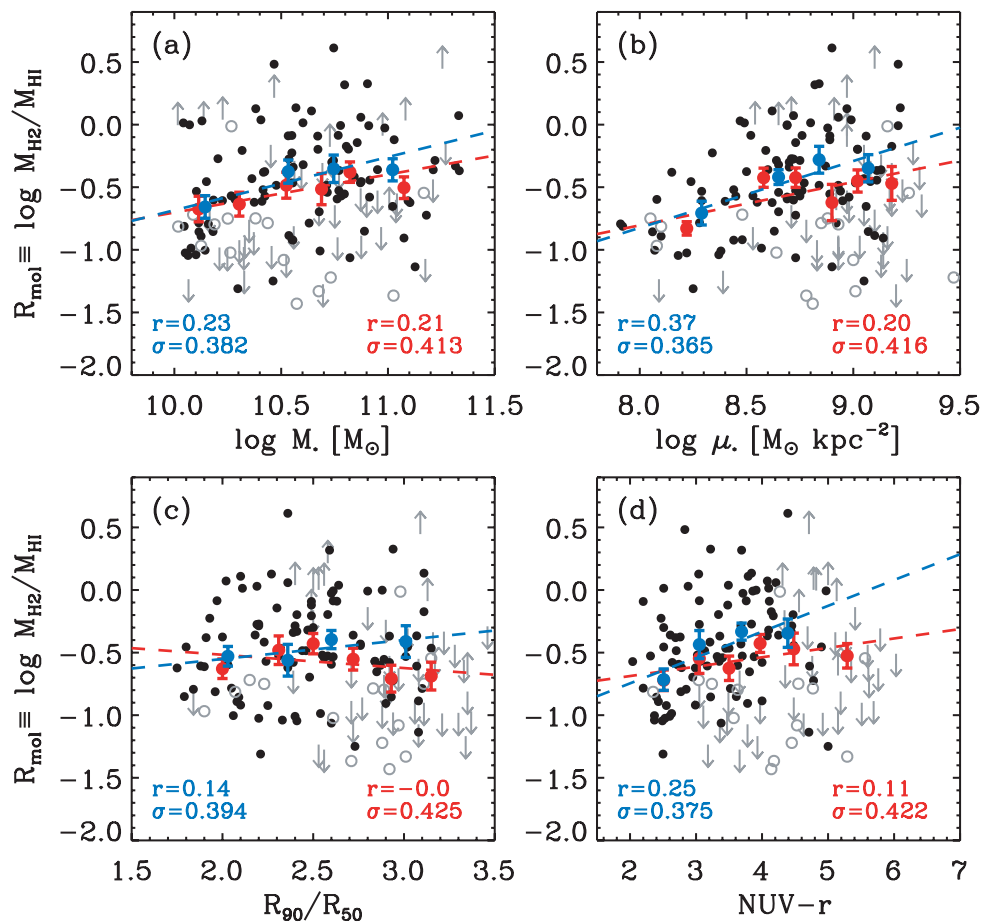


Figure 9. Molecular to atomic gas mass ratio as a function of (a) stellar mass, (b) stellar mass surface density, (c) concentration index R_{90}/R_{50} and (d) NUV – r colour. Detections in CO are shown as circles (filled: S/N > 5, open: S/N < 5), non-detections as upper limits. Non-detections in H I but with a CO detection are shown as lower limits. The mean scaling relations are also overplotted, with symbols as described in Fig. 7.

Table 4. Molecular-to-atomic gas mass ratio relations.

x	x_0	(1) Detections only		(2) All, non-detections = limit	
		m	b	m	b
$\log M_*$	10.70	0.425 ± 0.097	-0.387 ± 1.464	0.303 ± 0.084	-0.489 ± 1.253
$\log \mu_*$	8.70	0.533 ± 0.128	-0.451 ± 1.562	0.346 ± 0.142	-0.562 ± 1.772
R_{90}/R_{50}	2.50	0.152 ± 0.031	-0.475 ± 0.113	-0.106 ± 0.098	-0.571 ± 0.367
NUV – r	3.50	0.206 ± 0.057	-0.436 ± 0.289	0.075 ± 0.032	-0.575 ± 0.169

Note. The relations are parametrized as $\log M_{\text{H}_2}/M_{\text{H}_1} = m(x - x_0) + b$.

included, the slope of the relation is positive at the 3σ significance level (see Table 4). As demonstrated previously, f_{H_2} does not appear to depend significantly on M_* (Fig. 5a), while f_{H_1} is a fairly strongly declining function of M_* (Catinella et al. 2010). The combination of these two trends produces the weak increase in R_{mol} as a function of stellar mass.

Catinella et al. (2010) also reported a strong anticorrelation of f_{H_1} with the stellar mass surface density, μ_* . For galaxies with CO detections, the values of f_{H_2} show a similar but considerably weaker trend as a function of μ_* . In their resolved study, Leroy et al. (2008) show that the molecular-to-atomic ratio is a strong function of local properties within the discs of spiral galaxies. In particular, they find a dependence on stellar mass surface density, with the molecular fraction steadily increasing from surface mass densities

of $10^{7.5}$ to $10^9 M_{\odot} \text{ kpc}^{-2}$. Our molecular fractions are smaller because our measurements are integrated over entire galaxies, but the same qualitative trend is observed for our global measurements.

Even though f_{H_1} and f_{H_2} show different dependencies on μ_* , the fraction of galaxies with non-detections as a function of μ_* in the H I and CO samples exhibits very similar behaviour. As shown in Fig. 5(b) and in Catinella et al. (2010), there is a critical mass surface density of $\mu_* = 10^{8.7} M_{\odot} \text{ kpc}^{-2}$ below which all galaxies have a sizeable H I and H₂ component, and above which cold gas seems to have mostly disappeared. There are similar thresholds in concentration index and NUV – r colour (see e.g. our detection fractions in Fig. 2). However, while the mean value of f_{H_1} never falls below ~ 2 per cent, even at high μ_* or NUV – r colour (Fabello et al. 2011), f_{H_2} drops sharply below that level, as shown in Fig. 7

and evidenced by the results of our stacking experiment (Fig. 6). Furthermore, even though Catinella et al. (2010) found some red sequence galaxies with a surprisingly large H I component, none of these galaxies has a sizeable molecular gas mass; none of the galaxies with $\text{NUV} - r > 5$ is securely detected in CO. It therefore seems that above our empirical thresholds in μ_* , concentration index and $\text{NUV} - r$ colour, an increasing fraction of galaxies with any form of cold gas at all *appears to be dominated by atomic gas*. This result is also striking in Fig. 9(c), where we see the same population of atomic-gas dominated galaxies (i.e. the upper limits in R_{mol}) almost exclusively at $C > 2.6$. We note that this critical value of concentration index ($C = 2.6$) corresponds to the observed transition between late- and early-type galaxies (e.g. Shimasaku et al. 2001; Nakamura et al. 2003; Weinmann et al. 2009).

Finally, Fig. 9(d) shows that R_{mol} is an increasing function ($r = 0.25$) of $\text{NUV} - r$ colour for galaxies with detections of both H I and CO. Catinella et al. (2010) reported a strong anticorrelation between H I mass fraction and colour. Fig. 5(d) shows that there is also a fairly strong anticorrelation between f_{H_2} and $\text{NUV} - r$ colour. The fact that the anticorrelation of f_{H_1} with $\text{NUV} - r$ appears to ‘win’ probably reflects the fact that H I is dominant in regions such as outer galaxy discs where dust content is low and most of the starlight emitted by forming populations is emitted at UV wavelengths, whereas molecular gas tends to occur in the inner regions of galaxies where dust content is high and much of the light from young stars may be emitted in the infrared. In future work, we plan to look more carefully at these issues.

7 COMPARISON WITH PREVIOUS WORK

To put the new COLD GASS results in context, we assembled CO data from the literature for 263 nearby galaxies in the SDSS survey. They are taken from the compilations of Bettoni, Galletta & García-Burillo (2003), Yao et al. (2003), Casasola, Bettoni & Galletta (2004), Albrecht, Krügel & Chini (2007), Komugi et al. (2008) and Obreschkow & Rawlings (2009). When multiple measurements are found for the same galaxy, the newest is assumed to supersede previous values. The values of M_{H_2} were then homogenized to the best of our ability using a common conversion factor [$X_{\text{CO}} = 2.3 \times$

$10^{20} \text{ cm}^{-2} (\text{K km s}^{-1})^{-1}$] and cosmology ($H_0 = 70 \text{ km s}^{-1} \text{ Mpc}^{-1}$). In addition, the SDSS photometry was reprocessed using the same technique used for the COLD GASS galaxies (see Section 3), and used to measure reliable and homogeneous stellar masses.

In Fig. 10(a), we show the relation between M_{H_2}/M_* and M_* in this reference sample. The molecular gas mass fraction has a spread of more than 2 orders of magnitude, and does not appear to correlate with stellar mass. A significant fraction of this observed scatter can be attributed to measurement errors and inhomogeneities in the sample. The vast majority of these galaxies have $z < 0.02$, and therefore tend to be significantly larger than the typical observing beam, resulting in important aperture problems. Additional contributions to the artificially large scatter include different telescope calibrations, low S/N detections and selection on IR luminosity, which tends to bias f_{H_2} high.

As a comparison, we also show as contours in Fig. 10(a) the relations produced by Fu et al. (2010) through semi-analytic modelling of galaxy formation including detailed prescriptions for the break-up of gas between the atomic and molecular phases. The models predict a significantly smaller range in M_{H_2}/M_* than seen in the literature compilation. But it is also clear that a systematically measured set of galaxies will produce more consistent results, for example the THINGS/HERACLES sample (Walter et al. 2008; Leroy et al. 2009), which is also shown for comparison in Fig. 10.

The equivalent relation from COLD GASS is plotted in Fig. 10(b), showcasing the significantly reduced observational scatter compared to the literature compilation, but the increased dynamic range due to the rigorously measured upper limits for the CO non-detections. We note that the COLD GASS and HERACLES galaxies span a similar region in the plots. The HERACLES galaxies provide resolved CO maps for a much smaller sample of galaxies, so the two approaches are highly complementary.

The main results presented in this paper are overall qualitatively similar to some earlier observations. For example, Sage (1993) found that $M_{\text{H}_2}/M_{\text{dyn}}$ is independent of morphology, just like we find M_{H_2}/M_* to be independent of concentration index. However, they found that $M_{\text{H}_2}/M_{\text{H}_1}$ is a strong function of Hubble type (see also Young et al. 1989), which we do not. Based on these studies, we would have expected to find a significant population of

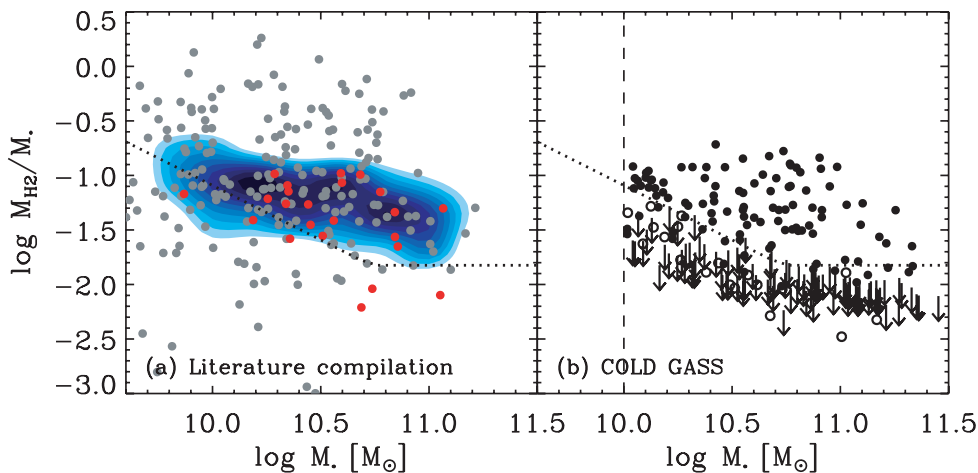


Figure 10. Left: relation between H₂ mass fraction and stellar mass for a compilation of 263 galaxies with CO measurements available from the literature (grey filled circles). The values of M_{H_2} have been homogenized for cosmology and the CO-to-H₂ conversion factor, but even with these corrections a scatter of more than 2 orders of magnitude is observed. This is in strong contrast with predictions from the models of Fu et al. (2010) (contours), and smaller but more homogeneous data sets (e.g. Leroy et al. 2009, shown as red circles). Right: in comparison, we show the same plot for the COLD GASS sample, with our minimum stellar mass selection (vertical dashed line) and our integration limit (dotted line) indicated.

early-type galaxies with large values of $M_{\text{H}_2}/M_{\text{H I}}$. We see no evidence for such systems in our sample.

Much of the earlier work regarding CO in nearby galaxies focused on the trends between M_{H_2} , $M_{\text{H I}}$ and morphology, interaction state (e.g. Braine & Combes 1993) or far-infrared properties of the systems (e.g. Sanders & Mirabel 1985). Using a set of galaxies still mostly based on the infrared-based FCRAO sample, Bothwell, Kennicutt & Lee (2009), however, derive relations similar to ours, between gas fraction (atomic and molecular) and B -band luminosity. Their findings are qualitatively similar to ours; they see that $M_{\text{H I}}/M_*$ decreases with luminosity, but M_{H_2}/M_* does not. The breakthrough here is that COLD GASS allows us to *quantitatively* describe, in an unbiased sample, how the molecular gas component varies with several key physical parameters which are at the basis of the theoretical effort towards understanding the star formation process.

8 SUMMARY

We are conducting COLD GASS, a legacy survey for molecular gas in nearby galaxies. We target at least 350 massive galaxies ($M_* > 10^{10} M_\odot$) in the CO(1–0) emission line with the IRAM 30-m telescope. Because the survey is unbiased, it will provide us with a complete view of the molecular gas properties of massive galaxies in the local Universe, as well as the relations between molecular gas and other global galaxy properties. The stellar mass and redshift ranges also ensure that we recover the total CO line flux of the galaxies with a single pointing of the IRAM 30-m telescope, and that a single CO luminosity to M_{H_2} conversion factor is likely adequate. Finally, our observations provide stringent upper limits on molecular gas fraction $M_{\text{H}_2}/M_* < 0.015$ in the case of CO non-detections.

In this paper, we present a catalogue of CO(1–0) fluxes and H_2 masses (or upper limits) for the first 222 galaxies observed as a part of COLD GASS, and report on their properties as follows.

(i) The detected molecular gas mass fractions (M_{H_2}/M_*) are in the range of 0.9–20 per cent, with a mean value $\langle M_{\text{H}_2}/M_* \rangle = 0.066 \pm 0.039$. The mean gas mass fraction among the *detected* galaxies does not vary strongly with any global galaxy property except colour.

(ii) We detect the CO(1–0) line in ~ 50 per cent of COLD GASS galaxies, and while the detection rate is independent of stellar mass, it is a strongly decreasing function of stellar mass surface density, concentration index and NUV – r colour. None of the 68 galaxies redder than NUV – $r = 5$ was detected, and stacking them leads to a non-detection and a stringent upper limit of $\langle M_{\text{H}_2}/M_* \rangle = 0.0016 \pm 0.0005$.

(iii) The mean molecular gas mass fraction (averaged over galaxies with detections and non-detections of the CO line) is a roughly constant function of stellar mass, but a decreasing function of stellar mass surface density and concentration index. The observed trends are weaker than those observed by Catinella et al. (2010) for the atomic gas mass fraction in a similar sample of galaxies. Of all the parameters investigated here, the molecular gas correlates most strongly with NUV – r colour, which is a tracer of specific star formation.

(iv) The molecular-to-atomic mass ratio, R_{mol} , has a mean value of 30 per cent over the entire sample. It is a weakly increasing function of M_* ($r = 0.23$) and μ_* ($r = 0.37$).

One result that we wish to highlight is the existence of sharp thresholds in galaxy structural parameters such as stellar surface

mass density, below which most galaxies have measurable atomic and molecular gas components, but above which the detection rate of both the H I and CO lines drops drastically. This result was discussed previously for the H I in Catinella et al. (2010). The fact that *the same sharp thresholds also apply to the CO* strongly suggests that the onset of ‘quenching’ processes in galaxies was associated with a change in their structure. We note that the same sharp drop in cold gas content is not seen as a function of stellar mass. Intriguingly, atomic gas dominates in the minority of galaxies that are above threshold and that have a significant cold gas content. One possible interpretation is that the re-accretion of gas may still be possible following the quenching event. In future work, we will examine galaxies on either side of the ‘quenching threshold’ in more detail. We will also look more closely at the relationship between molecular gas content and star formation.

ACKNOWLEDGMENTS

This work is based on observations carried out with the IRAM 30-m telescope. IRAM is supported by INSU/CNRS (France), MPG (Germany) and IGN (Spain).

We are grateful to Nario Kuno for providing us with total fluxes for his sample of nearby galaxies. We wish to thank the staff of the IRAM observatory for their tremendous help in conducting our observations. We thank the anonymous referee for a constructive and helpful report.

RG and MPH are supported by NSF grant AST-0607007 and by a grant from the Brinson Foundation.

REFERENCES

- Abazajian K. N. et al., 2009, *ApJS*, 182, 543
 Abdo A. A. et al., 2010, *ApJ*, 710, 133
 Albrecht M., Krügel E., Chini R., 2007, *A&A*, 462, 575
 Bettoni D., Galletta G., García-Burillo S., 2003, *A&A*, 405, 5
 Bigiel F., Leroy A., Walter F., Brinks E., de Blok W. J. G., Madore B., Thornley M. D., 2008, *AJ*, 136, 2846
 Blitz L., Fukui Y., Kawamura A., Leroy A., Mizuno N., Rosolowsky E., 2007, *Protostars and Planets V*. Univ. Arizona Press, Tucson, AZ, p. 81
 Bolatto A. D., Leroy A. K., Rosolowsky E., Walter F., Blitz L., 2008, *ApJ*, 686, 948
 Boselli A., Gavazzi G., Lequeux J., Buat V., Casoli F., Dickey J., Donas J., 1997, *A&A*, 327, 522
 Boselli A., Lequeux J., Gavazzi G., 2002, *A&A*, 384, 33
 Bothwell M. S., Kennicutt R. C., Lee J. C., 2009, *MNRAS*, 400, 154
 Braine J., Combes F., 1993, *A&A*, 269, 7
 Braine J., Combes F., Casoli F., Dupraz C., Gerin M., Klein U., Wielebinski R., Brouillet N., 1993, *A&AS*, 97, 887
 Bruzual G., Charlot S., 2003, *MNRAS*, 344, 1000
 Casasola V., Bettoni D., Galletta G., 2004, *A&A*, 422, 941
 Casoli F., Boisse P., Combes F., Dupraz C., 1991, *A&A*, 249, 359
 Catinella B., Haynes M. P., Giovanelli R., 2007, *AJ*, 134, 334
 Catinella B. et al., 2010, *MNRAS*, 403, 683
 Chabrier G., 2003, *PASP*, 115, 763
 Combes F., Encrenaz P. J., Lucas R., Weliachew L., 1977, *A&A*, 55, 311
 Combes F., Young L. M., Bureau M., 2007, *MNRAS*, 377, 1795
 Dame T. M., Hartmann D., Thaddeus P., 2001, *ApJ*, 547, 792
 Dickman R. L., Snell R. L., Schloerb F. P., 1986, *ApJ*, 309, 326
 Draine B. T. et al., 2007, *ApJ*, 663, 866
 Dutton A. A., Conroy C., van den Bosch F. C., Simard L., Mendel J. T., Courteau S., Dekel A., More S., Prada F., 2011, *MNRAS*, in press (arXiv:1012.5859, doi:10.1111/j.1365-2966.2011.19038.x)

Fabello S., Catinella B., Giovanelli R., Kauffmann G., Haynes M. P., Heckman T. M., Schiminovich D., 2011, *MNRAS*, 411, 993

Fu J., Guo Q., Kauffmann G., Krumholz M. R., 2010, *MNRAS*, 409, 515

Gao Y., Solomon P. M., 2004, *ApJ*, 606, 271

García-Burillo S. et al., 2003, *A&A*, 407, 485

Giovanelli R. et al., 2005, *AJ*, 130, 2598

Helfer T. T., Blitz L., 1993, *ApJ*, 419, 86

Heyer M., Krawczyk C., Duval J., Jackson J. M., 2009, *ApJ*, 699, 1092

Jorgensen I., Franx M., Kjaergaard P., 1996, *MNRAS*, 280, 167

Kenney J. D., Young J. S., 1988, *ApJS*, 66, 261

Kenney J. D. P., Young J. S., 1989, *ApJ*, 344, 171

Kennicutt R. C., Jr, 1998, *ApJ*, 498, 541

Keres D., Yun M. S., Young J. S., 2003, *ApJ*, 582, 659

Komugi S., Sofue Y., Kohno K., Nakanishi H., Onodera S., Egusa F., Muraoka K., 2008, *ApJS*, 178, 225

Krips M., Crocker A. F., Bureau M., Combes F., Young L. M., 2010, *MNRAS*, 407, 2261

Kuno N. et al., 2007, *PASJ*, 59, 117

Leroy A. K., Walter F., Brinks E., Bigiel F., de Blok W. J. G., Madore B., Thornley M. D., 2008, *AJ*, 136, 2782

Leroy A. K. et al., 2009, *AJ*, 137, 4670

Martin D. C. et al., 2005, *ApJ*, 619, L1

Moran S. M. et al., 2010, *ApJ*, 720, 1126

Nakamura O., Fukugita M., Yasuda N., Loveday J., Brinkmann J., Schneider D. P., Shimasaku K., SubbaRao M., 2003, *AJ*, 125, 1682

Obreschkow D., Rawlings S., 2009, *MNRAS*, 394, 1857

Radford S. J. E., Downes D., Solomon P. M., 1991, *ApJ*, 368, L15

Regan M. W., Thornley M. D., Helfer T. T., Sheth K., Wong T., Vogel S. N., Blitz L., Bock D., 2001, *ApJ*, 561, 218

Rickard L. J., Palmer P., Morris M., Zuckerman B., Turner B. E., 1975, *ApJ*, 199, L75

Sage L. J., 1993, *A&A*, 272, 123

Saintonge A. et al., 2011, *MNRAS*, 415, 61 (this issue)

Sakamoto K., Okumura S. K., Ishizuki S., Scoville N. Z., 1999, *ApJ*, 525, 691

Salim S. et al., 2007, *ApJS*, 173, 267

Sanders D. B., Mirabel I. F., 1985, *ApJ*, 298, L31

Sanders D. B., Mirabel I. F., 1996, *ARA&A*, 34, 749

Sanders D. B., Scoville N. Z., Soifer B. T., 1991, *ApJ*, 370, 158

Schiminovich D. et al., 2010, *MNRAS*, 408, 919

Shimasaku K. et al., 2001, *AJ*, 122, 1238

Solomon P. M., de Zafra R., 1975, *ApJ*, 199, L79

Solomon P. M., Downes D., Radford S. J. E., Barrett J. W., 1997, *ApJ*, 478, 144

Springob C. M., Haynes M. P., Giovanelli R., Kent B. R., 2005, *ApJS*, 160, 149

Stoughton C. et al., 2002, *AJ*, 123, 485

Strong A. W., Mattox J. R., 1996, *A&A*, 308, L21

Tacconi L. J. et al., 2008, *ApJ*, 680, 246

Tacconi L. J. et al., 2010, *Nat*, 463, 781

Thronson H. A., Jr, Tacconi L., Kenney J., Greenhouse M. A., Margulis M., Tacconi-Garman L., Young J. S., 1989, *ApJ*, 344, 747

Tremonti C. A. et al., 2004, *ApJ*, 613, 898

Tully R. B., Fisher J. R., 1977, *A&A*, 54, 661

Verter F., 1985, *ApJS*, 57, 261

Walter F., Brinks E., de Blok W. J. G., Bigiel F., Kennicutt R. C., Thornley M. D., Leroy A., 2008, *AJ*, 136, 2563

Wang J., Overzier R., Kauffmann G., von der Linden A., Kong X., 2010, *MNRAS*, 401, 433

Weinmann S. M., Kauffmann G., van den Bosch F. C., Pasquali A., McIntosh D. H., Mo H., Yang X., Guo Y., 2009, *MNRAS*, 394, 1213

Wiklund T., Henkel C., 1989, *A&A*, 225, 1

Wyder T. K. et al., 2007, *ApJS*, 173, 293

Yao L., Seaquist E. R., Kuno N., Dunne L., 2003, *ApJ*, 588, 771

Young J. S., Knezek P. M., 1989, *ApJ*, 347, L55

Young J. S., Xie S., Kenney J. D. P., Rice W. L., 1989, *ApJS*, 70, 699

Young J. S. et al., 1995, *ApJS*, 98, 219

APPENDIX A: SPECTRAL GALLERY

A1 Galaxies with CO line detections

In Fig A1, we present the SDSS imaging and IRAM spectra for the COLD GASS galaxies present in this data release for which we have securely detected the CO(1–0) line. These are defined as those with $S/N > 5$ in the CO line. The tentative detections, those with $S/N < 5$, are shown in Fig A2. All galaxies with a secure CO line detection have colours bluer than $NUV - r = 5.0$, but cover uniformly the stellar mass range probed by COLD GASS.

A2 Galaxies with non-detection of the CO line

For completeness, we show in Fig A3 the SDSS three-colour images of the CO non-detections. These objects tend to be red ($NUV - r > 5$), early-type-looking ($C > 2.6$) galaxies.

A3 Offset pointings

As described in Section 4.4, we perform additional off-centre pointings for a small fraction of the COLD GASS sources. They are the larger galaxies ($D_{25} > 40$ arcsec), with a strong detection in the central pointing. These offsets are taken 16 arcsec (or three quarters of the main beam) away from the centres. In Fig A4, we show the SDSS images and IRAM spectra for the offset pointings. The data reduction process is identical to that used for the central pointings and described in Section 4.3. The emission lines are identified by examining the spectra at the expected positions based on the redshift on each galaxy, and the width of CO the line in the central pointing is used as additional information. Fluxes are measured by integrating over the region identified through this process, and the flux ratio between offset and central pointings is used to determine an appropriate aperture correction for each galaxy using the technique described in Section 4.4.

SUPPORTING INFORMATION

Additional Supporting Information may be found in the online version of this article:

Table 1. Optical and UV parameters of the COLD GASS galaxies.
Table 2. Molecular gas masses and CO(1–0) parameters for the COLD GASS galaxies.

Please note: Wiley-Blackwell are not responsible for the content or functionality of any supporting materials supplied by the authors. Any queries (other than missing material) should be directed to the corresponding author for the article.

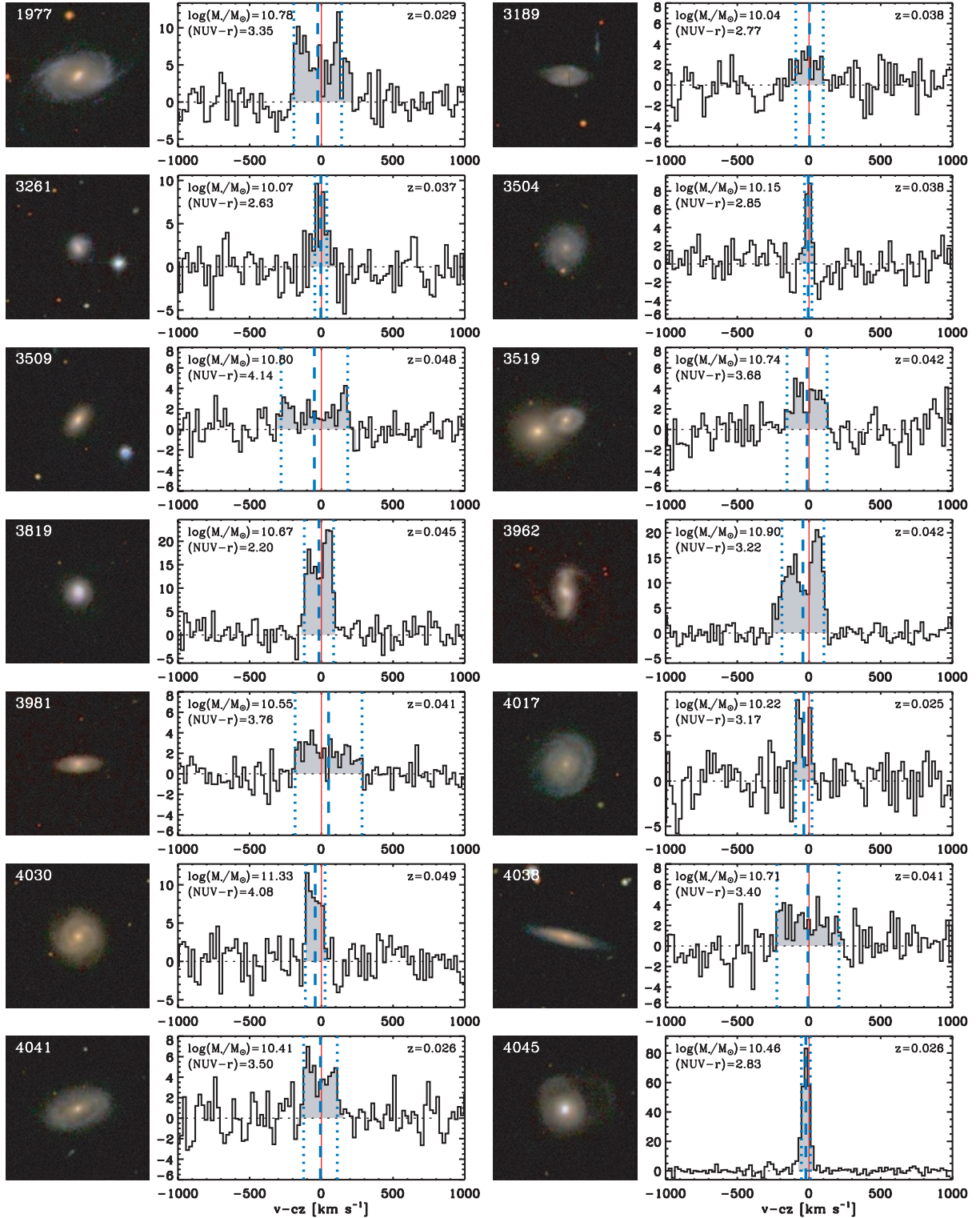


Figure A1. SDSS three-colour image ($1.5 \times 1.5 \text{ arcmin}^2$) and CO(1–0) line spectrum of COLD GASS targets with a secure detection ($S/N > 5$). The solid red line shows the systemic redshift of the galaxy as determined from the SDSS fibre spectra. The dashed blue line is the central velocity of the CO line, and the interval delimited by the two dotted blue lines is $W50_{\text{CO}}$, the full linewidth of the CO emission measured at half intensity.

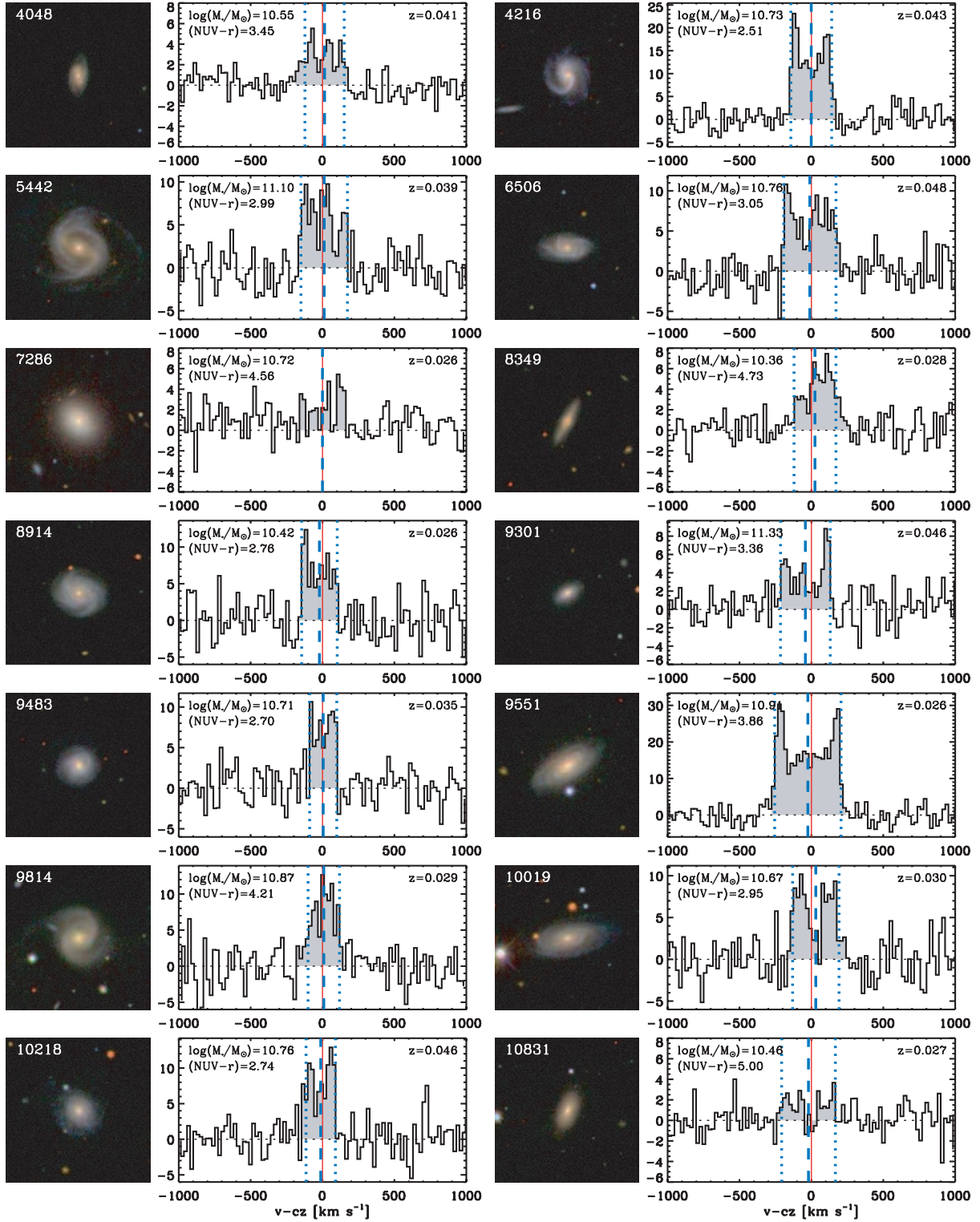


Figure A1 – *continued*

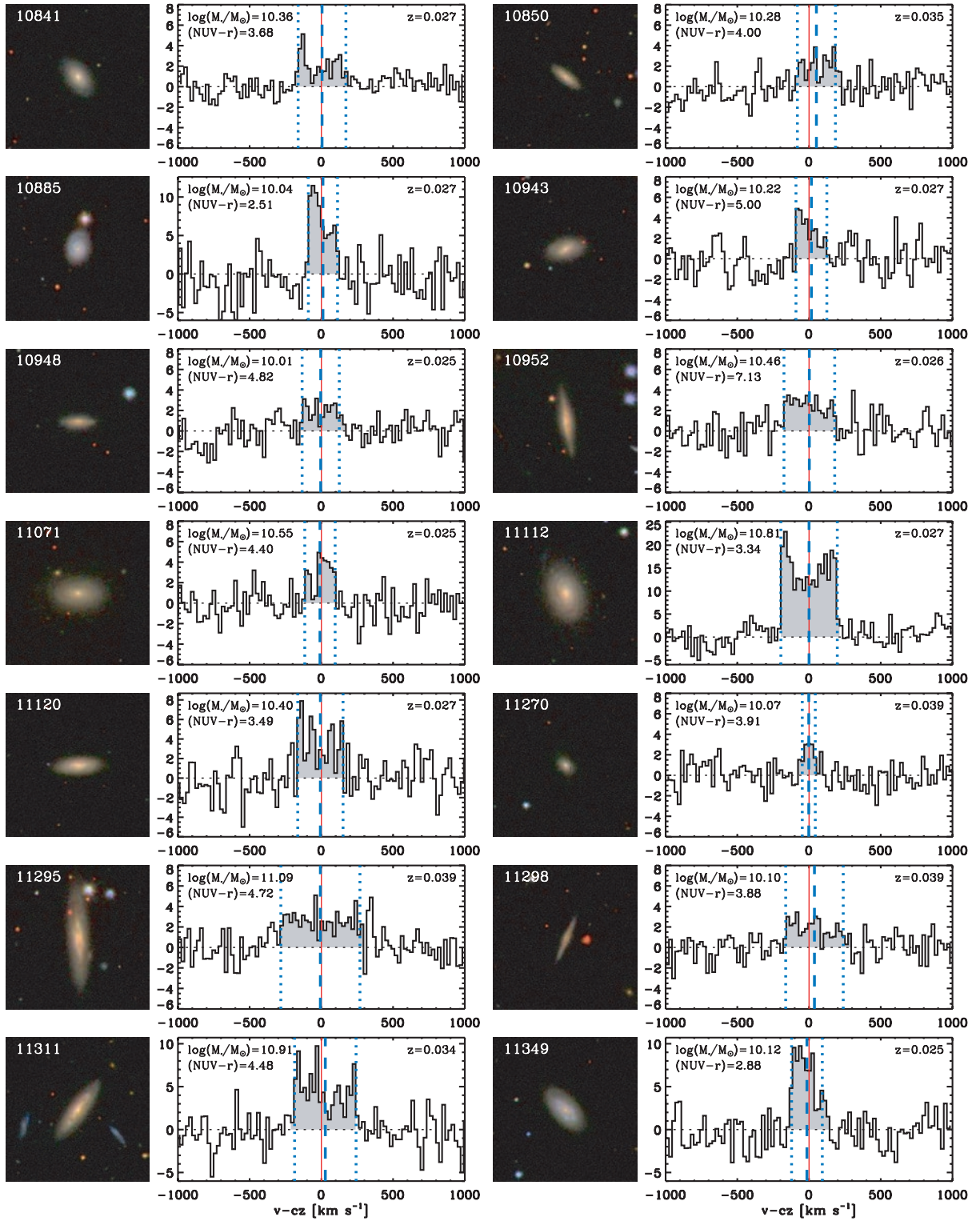
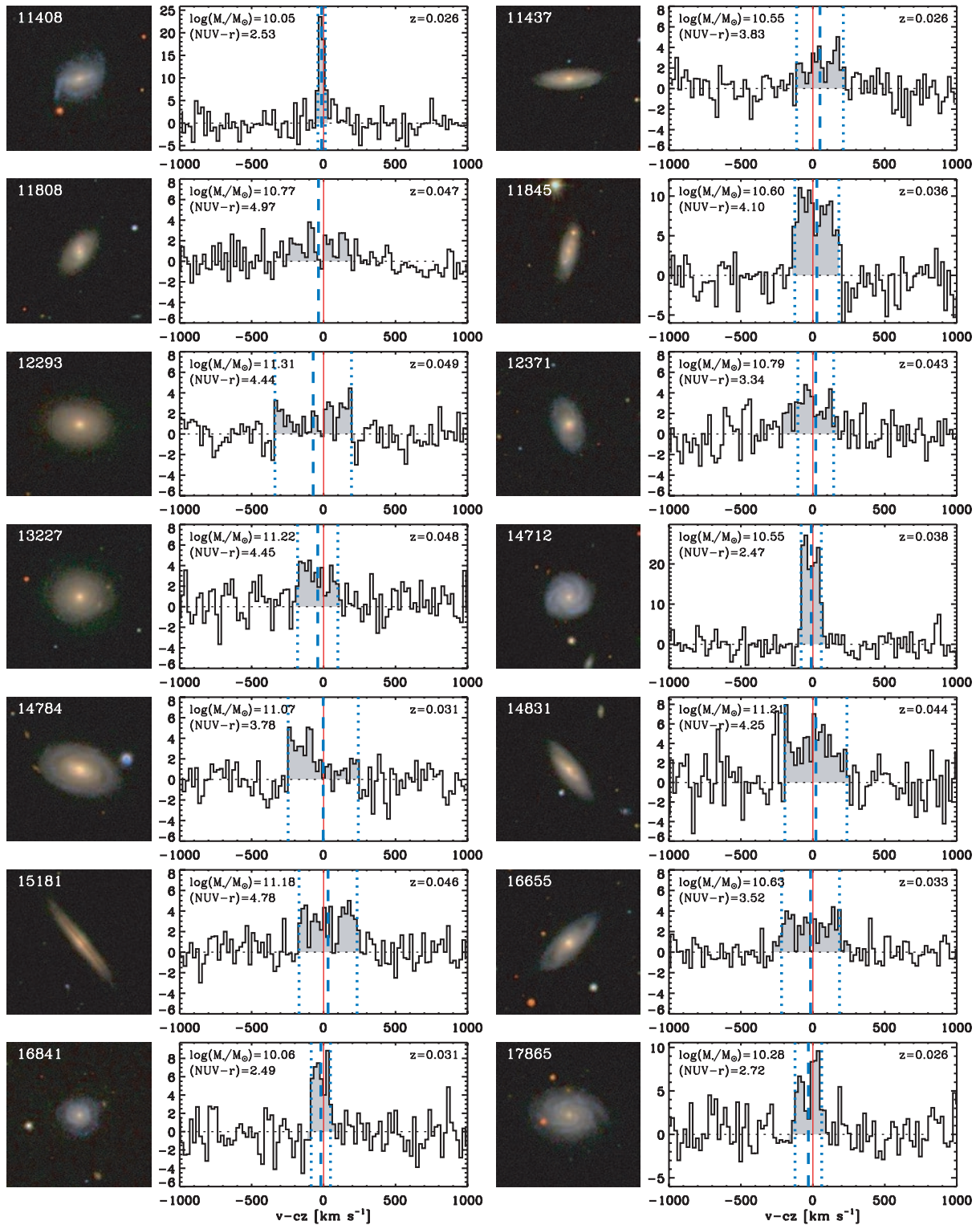


Figure A1 – continued

Figure A1 – *continued*

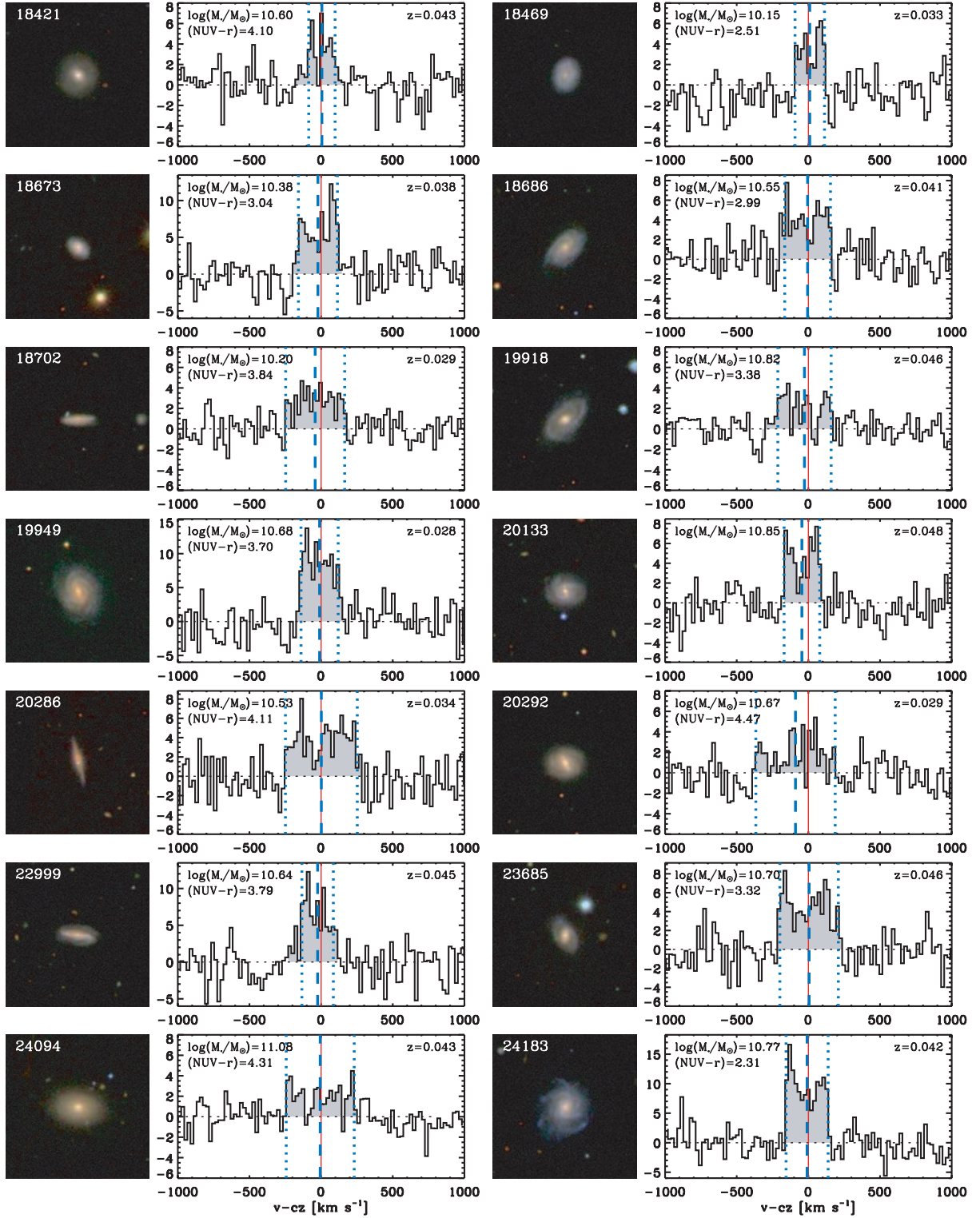
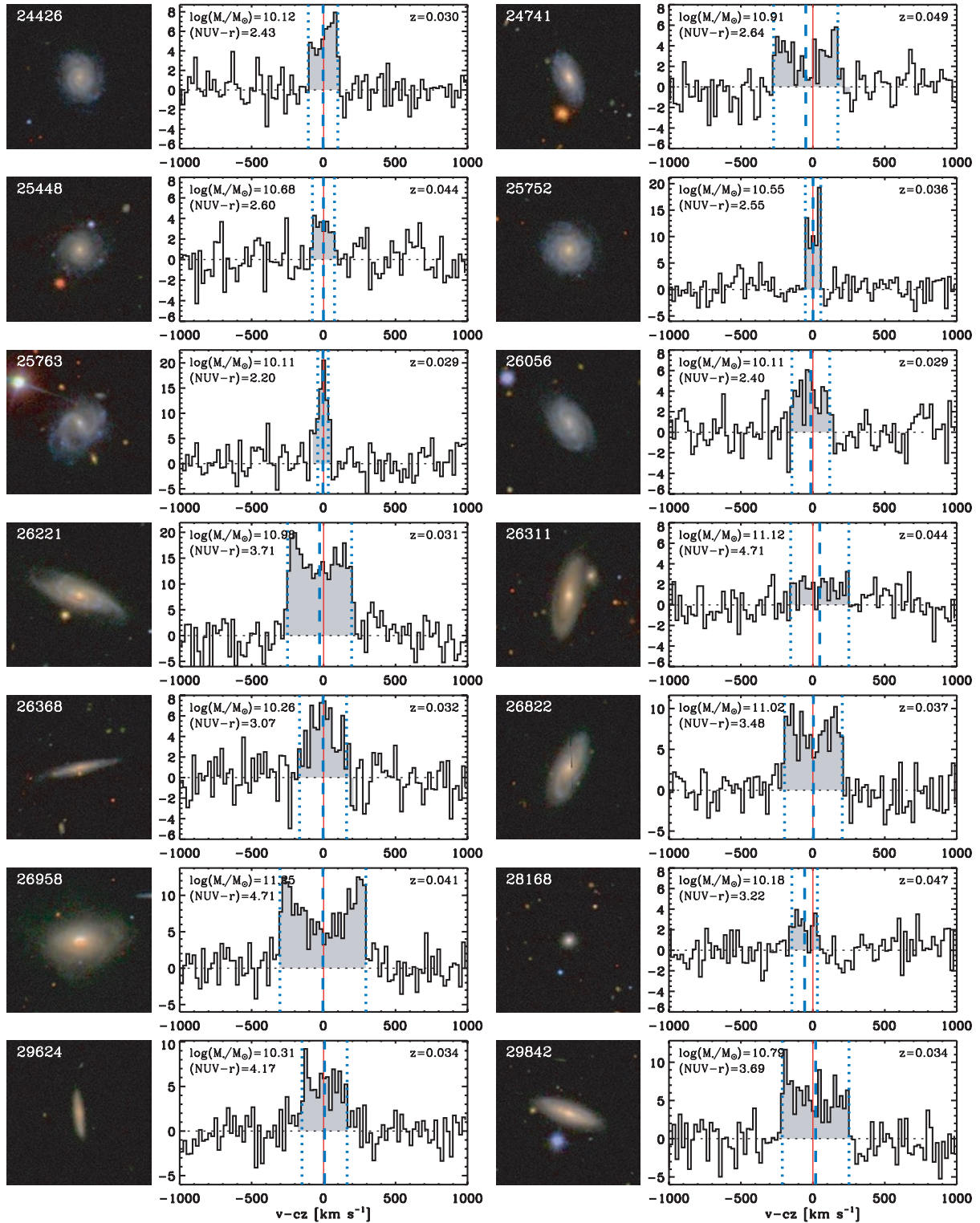


Figure A1 – continued

Figure A1 – *continued*

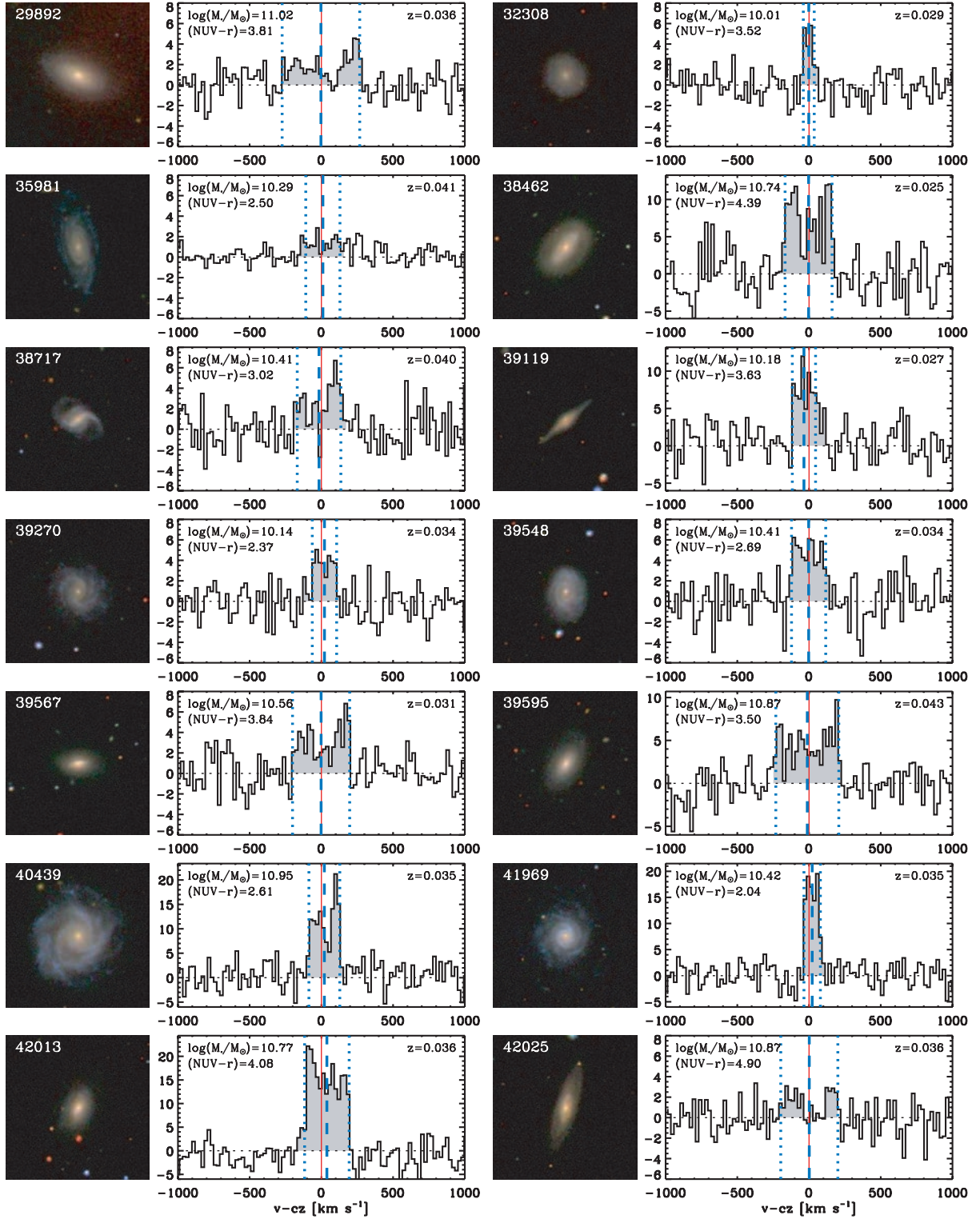


Figure A1 – continued

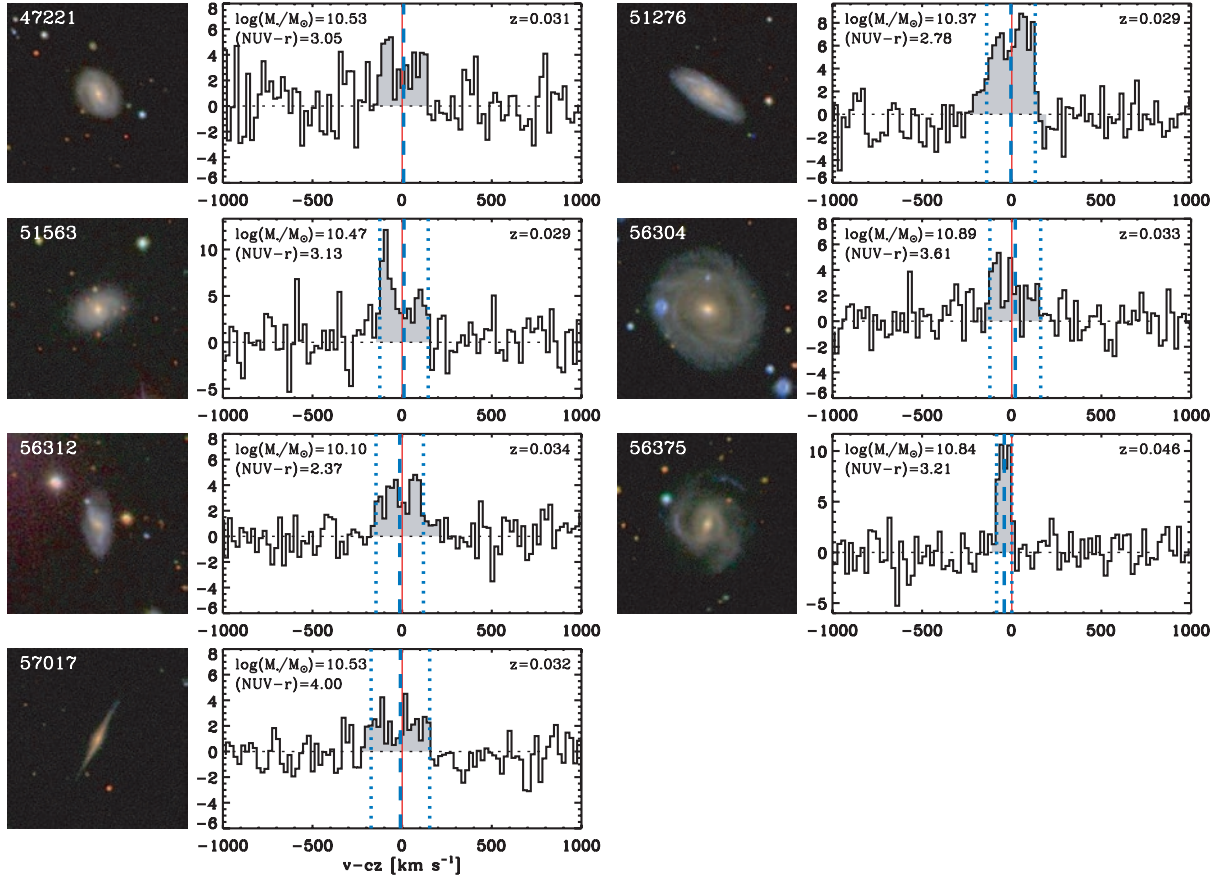


Figure A1 – continued

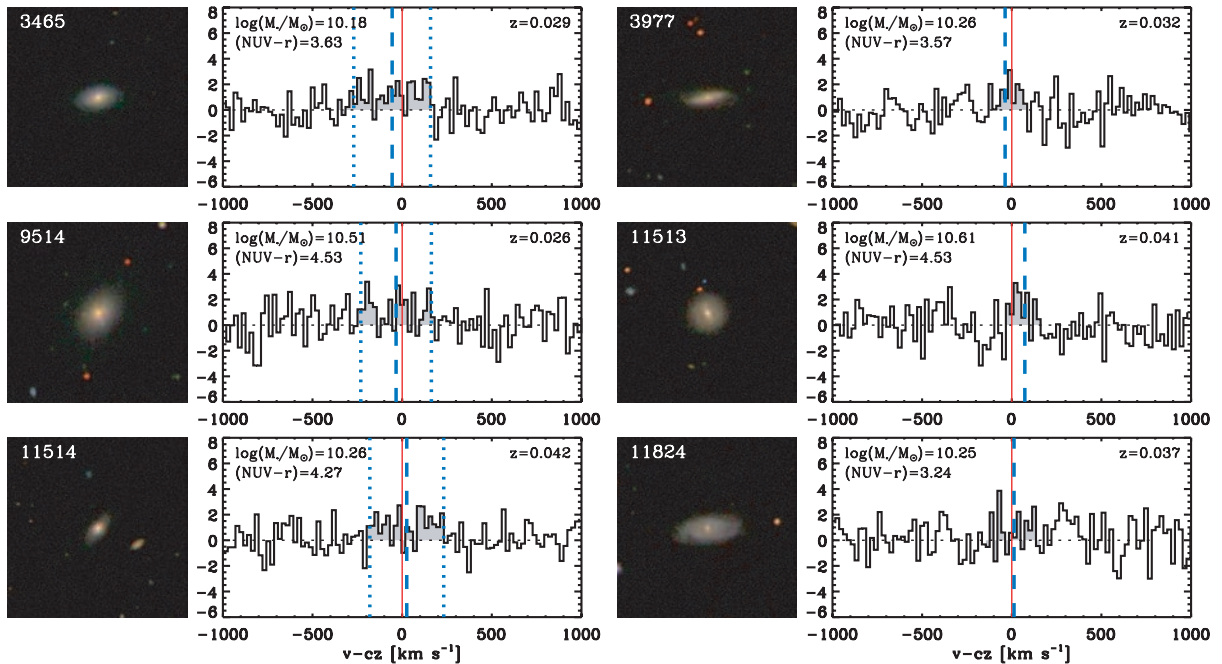


Figure A2. SDSS three-colour image and CO(1–0) line spectrum of COLD GASS targets with a tentative detection ($S/N < 5$). Lines are as described in the caption of Fig. A1. Given the low S/N of these detections, the width determination is sometimes poor, and in these cases the corresponding vertical dotted lines are omitted.

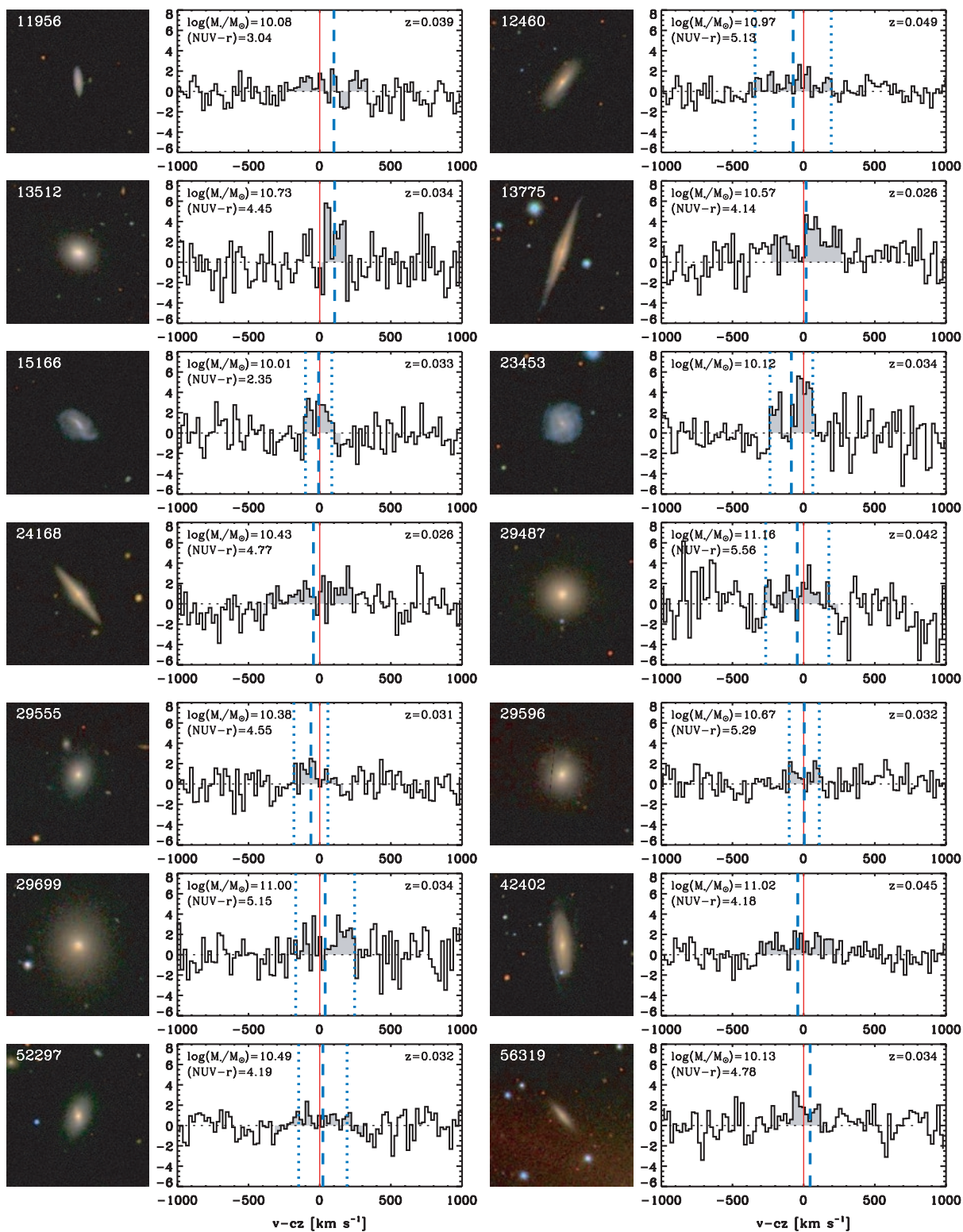


Figure A2 – continued

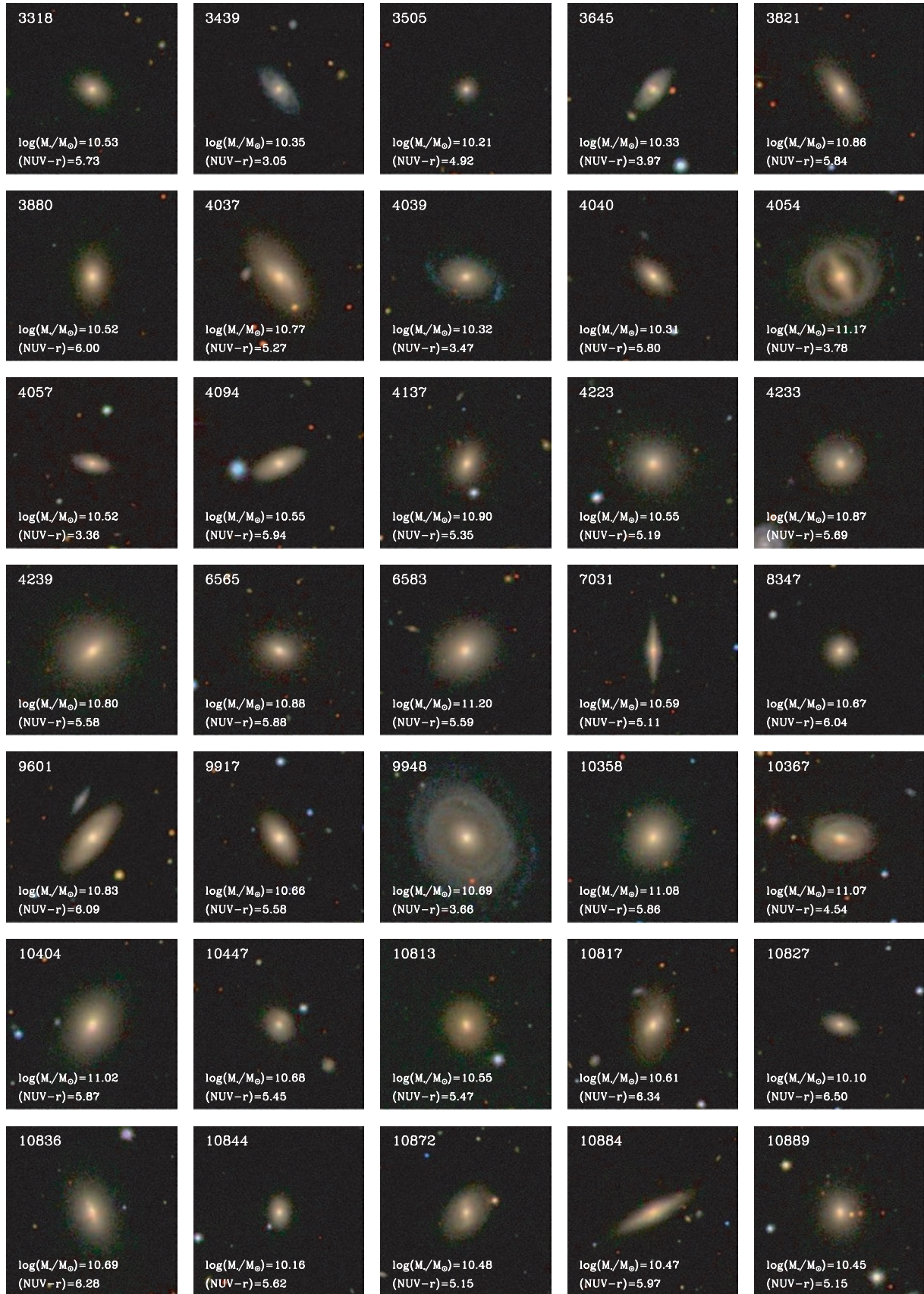


Figure A3. SDSS three-colour images of COLD GASS galaxies where the CO(1–0) line is not detected. Each image has a size of 1.5×1.5 arcmin².

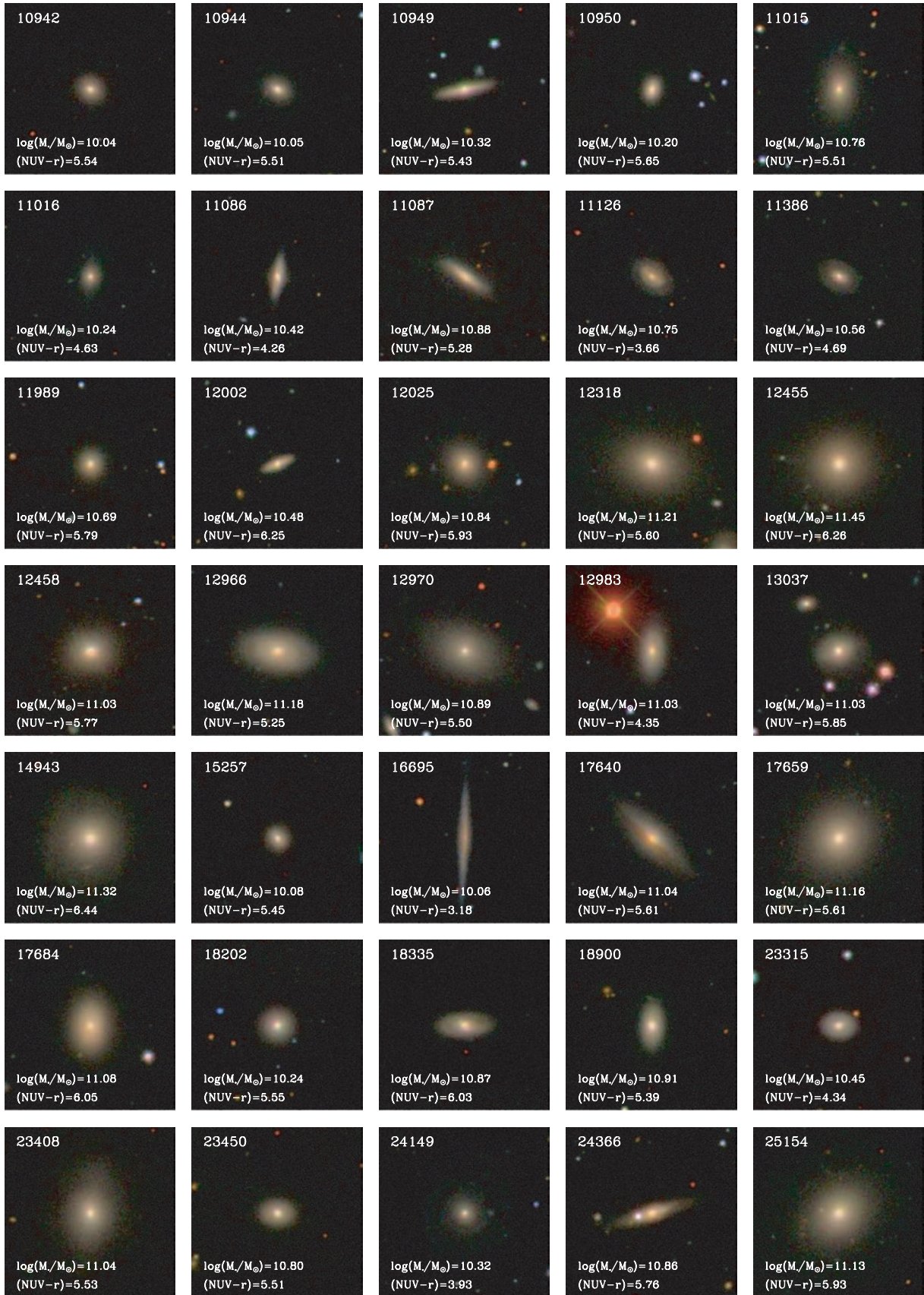
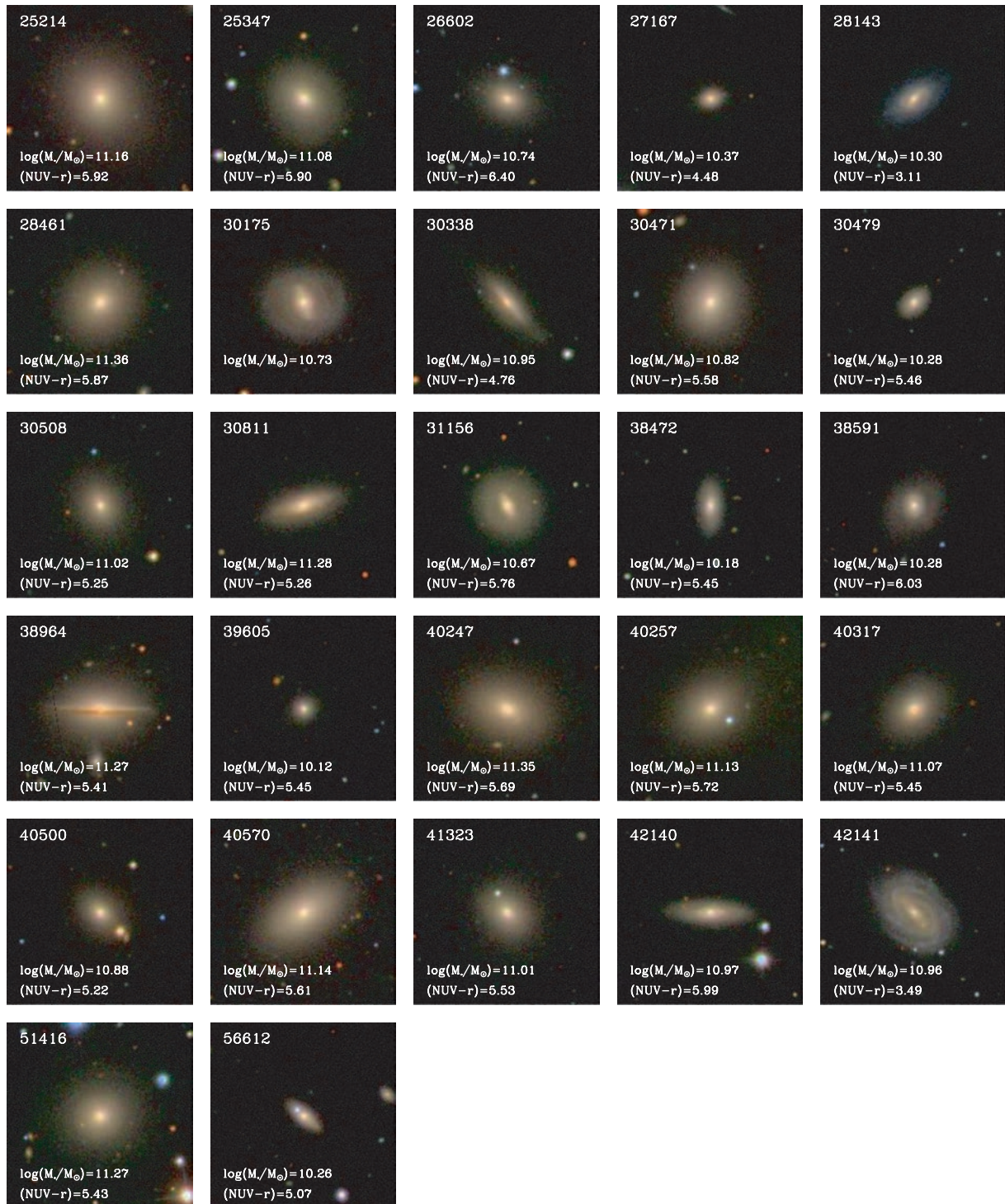


Figure A3 – continued

Figure A3 – *continued*

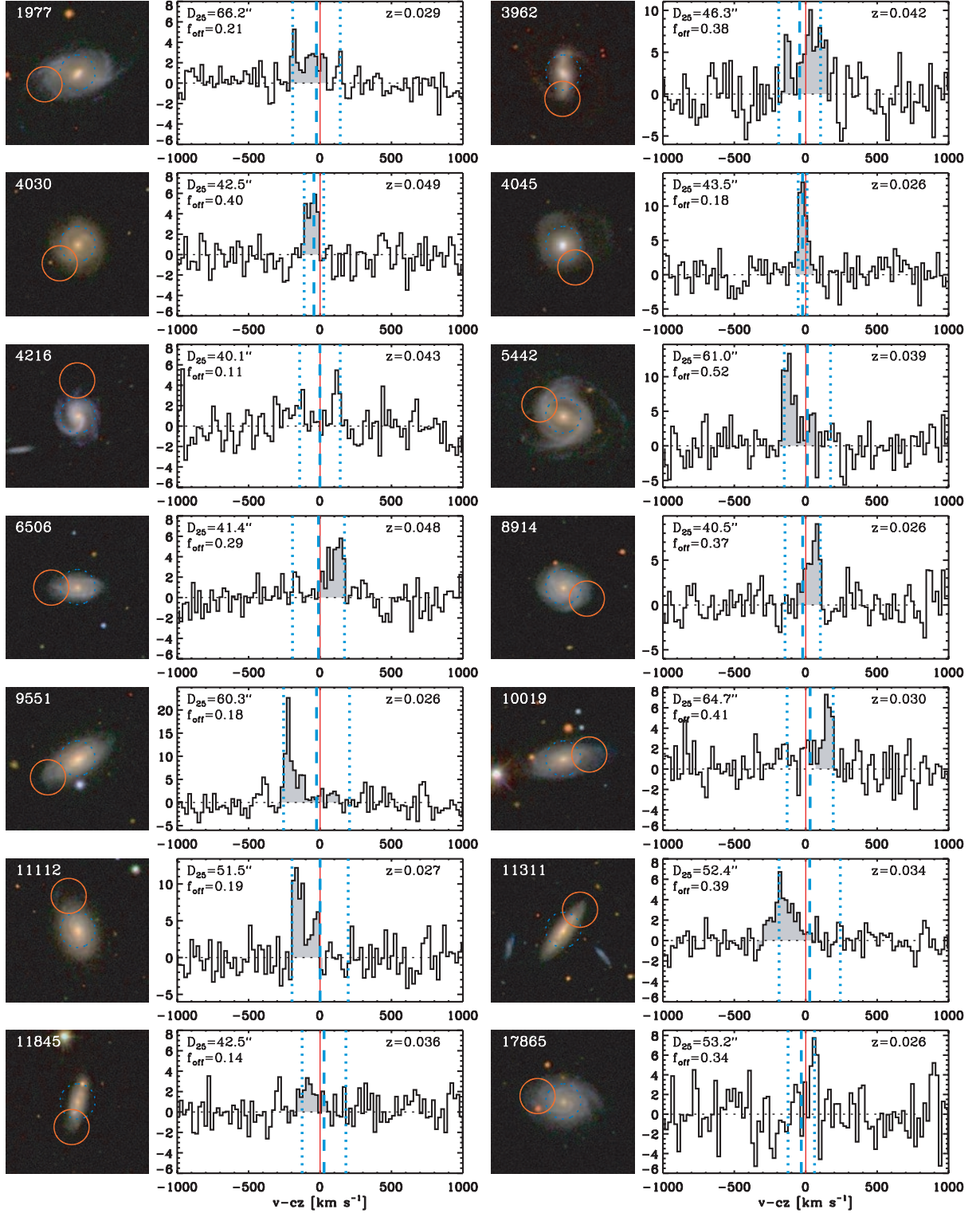
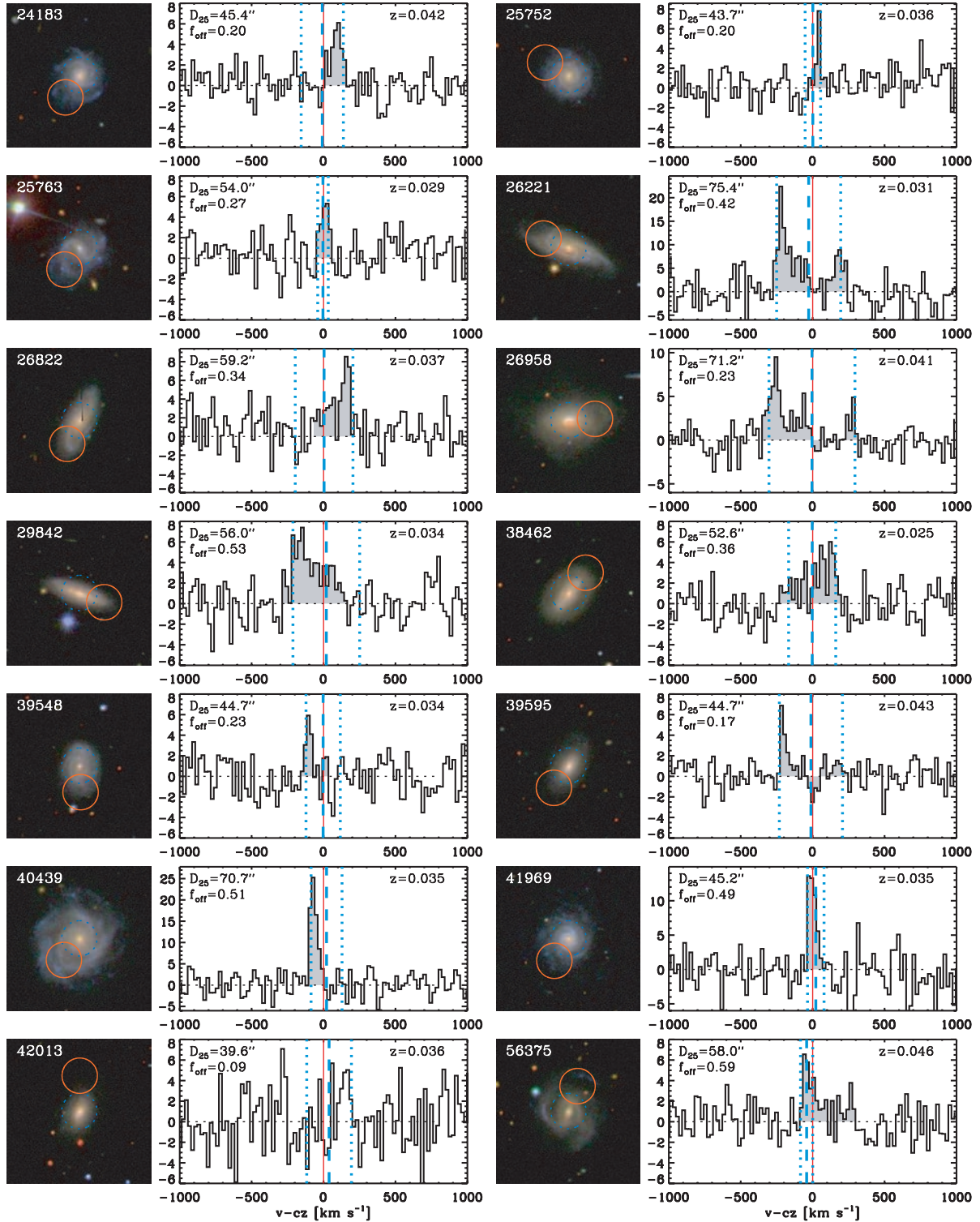


Figure A4. SDSS three-colour image and CO(1–0) line spectrum measured in offset pointings on COLD GASS galaxies. The blue circle shows the central position of the 22-arcsec beam, and the orange circle the offset position, located three quarters of a beam from the centre (for G1977, G4216, G9551, G11112 and G42013, the offset was taken one full beam away from the centre; see Section 4.4). On the spectra, we overplot the optical redshift of the galaxies (red lines), and the central position and widths of the line detected in the *central* pointings (blue lines). The shaded region shows the region of the offset spectrum integrated to measure the line flux. The optical diameter from SDSS *g*-band imaging (D_{25}) and the flux ratio between offset and central pointings (f_{off}) are given in each case.

Figure A4 – *continued*

This paper has been typeset from a $\text{\TeX}/\text{\LaTeX}$ file prepared by the author.